AFRL-AFOSR-JP-TR-2019-0012

Ultrastrong Carbon Thin Films from Diamond to Graphene under Extreme Conditions: Probing Atomic-Scale Interfacial Mechanisms to Achieve Ultralow Friction and Wear

Reau-Ren Jeng
NATIONAL CHUNG CHENG UNIVERSITY
160 SAN-HSING
MIN-HSIUNG, CHIA-YI, 621
TW

03/19/2019
Final Report

DISTRIBUTION A: Distribution approved for public release.

Air Force Research Laboratory
Air Force Office of Scientific Research
Asian Office of Aerospace Research and Development
Unit 45002, APO AP 96338-5002

REPORT DOCUMENTATION PAGE

Form Approved
OMB No. 0704-0188

The public reporting burden for this collection of information is estimated to average 1 hour per response, including the time for reviewing instructions, searching existing data sources, gathering and maintaining the data needed, and completing and reviewing the collection of information. Send comments regarding this burden estimate or any other aspect of this collection of information, including suggestions for reducing the burden, to Department of Defense, Executive Services, Directorate (0704-0188). Respondents should be aware that notwithstanding any other provision of law, no person shall be subject to any penalty for failing to comply with a collection of information if it does not display a currently valid OMB control number.
PLEASE DO NOT RETURN YOUR FORM TO THE ABOVE ORGANIZATION.

1. REPORT DATE *(DD-MM-YYYY)*	2. REPORT TYPE	3. DATES COVERED *(From - To)*
19-03-2019	Final	28 Sep 2017 to 27 Sep 2018

4. TITLE AND SUBTITLE
Ultrastrong Carbon Thin Films from Diamond to Graphene under Extreme Conditions: Probing Atomic-Scale Interfacial Mechanisms to Achieve Ultralow Friction and Wear

5a. CONTRACT NUMBER

5b. GRANT NUMBER
FA2386-17-1-4002

5c. PROGRAM ELEMENT NUMBER
61102F

6. AUTHOR(S)
Reau-Ren Jeng

5d. PROJECT NUMBER

5e. TASK NUMBER

5f. WORK UNIT NUMBER

7. PERFORMING ORGANIZATION NAME(S) AND ADDRESS(ES)
NATIONAL CHUNG CHENG UNIVERSITY
160 SAN-HSING
MIN-HSIUNG, CHIA-YI, 621 TW

8. PERFORMING ORGANIZATION REPORT NUMBER

9. SPONSORING/MONITORING AGENCY NAME(S) AND ADDRESS(ES)
AOARD
UNIT 45002
APO AP 96338-5002

10. SPONSOR/MONITOR'S ACRONYM(S)
AFRL/AFOSR IOA

11. SPONSOR/MONITOR'S REPORT NUMBER(S)
AFRL-AFOSR-JP-TR-2019-0012

12. DISTRIBUTION/AVAILABILITY STATEMENT
A DISTRIBUTION UNLIMITED: PB Public Release

13. SUPPLEMENTARY NOTES

14. ABSTRACT
The project goal was to gain a fundamental understanding of how to achieve low friction and wear in ultrastrong carbon-based materials. Experimentally, an in situ nanotribometry method was used, which enables nanoscale visualization of sliding contacts inside the transmission electron microscope (TEM). These experiments are in turn modelled computationally using molecular dynamics, allowing better understanding of the atomic-scale processes controlling friction and wear. The focus was on the behavior of silicon-silicon, silicon-diamond, and diamond-like-carbon (DLC)-diamond interfaces. For silicon-silicon interfaces, nanocontacts showed a sliding-history and stress-dependent adhesion, where sliding increased adhesion by more than 16 times. This effect was enhanced by the applied normal stress. This is explained in terms of stress-activated covalent bond breaking that only occurs during sliding. For silicon in sliding contact with diamond, the observed adhesion increases with applied stress and speed. This dependence is explained in terms of tip geometry changes due to atomic-scale plasticity. For DLC interfaces, wear during sliding and the evolution of adhesion forces were characterized. Wear was measured as a function of load and sliding distance. Gradual wear with sliding was observed with the wear rate increasing with the average contact stress, but not following the classic Archards wear law nor to recently observed behavior following transition state theory. The wear behavior over the full range of stresses is well described by multi-bond wear model that exhibits a change from Archard-like behavior at high stresses to a transition state theory description at lower stresses. Adhesion showed large scatter, which was attributed to stochastic covalent bond breaking and formation events. In summary, this work shows that understanding adhesion and wear requires caref

15. SUBJECT TERMS
Tribology, Surfaces, Graphene, Diamond, Single Asperity, Ultrananocrystalline Diamond, Multiscale Simulations

16. SECURITY CLASSIFICATION OF:			17. LIMITATION OF ABSTRACT	18. NUMBER OF PAGES	19a. NAME OF RESPONSIBLE PERSON
a. REPORT	b. ABSTRACT	c. THIS PAGE			WINDER, SHEENA
Unclassified	Unclassified	Unclassified	SAR		19b. TELEPHONE NUMBER *(Include area code)* +81-42-511-2008

Standard Form 298 (Rev. 8/98)
Prescribed by ANSI Std. Z39.18

Final Report for AOARD Grant # FA2386-17-1-4002

"Ultrastrong Carbon Thin Films from Diamond to Graphene under Extreme Conditions: Probing Atomic-Scale Interfacial Mechanisms to Achieve Ultralow Friction and Wear"

Oct. 20, 2018

PI information:
Asia (Taiwan) Awardee
Yeau-Ren Jeng
E-mail: imeyrj@ccu.edu.tw
National Chung Cheng University (CCU)
Department of Mechanical Engineering,
Ming-Hsiung, Chia-Yi 621, Taiwan
Tel: 886-5-2428189 Fax: 886-5-2720589

Co-PI information:
U.S. Awardee
Robert W. Carpick
Email: carpick@seas.upenn.edu
University of Pennsylvania (Penn)
Mechanical Engineering and Applied Mechanics
229 Towne, 220 S. 33rd St., Philadelphia, PA, 19104-6315, USA
Tel: 215-898-4608 Fax: 215-573-6334

Period of Performance: 09/28/2017– 09/27/2018

Abstract: Our goal was to gain a fundamental understanding of how to achieve low friction and wear in ultrastrong carbon-based materials. Experimentally, we used an *in situ* nanotribometry method, which enables nanoscale visualization of sliding contacts inside the transmission electron microscope (TEM). These experiments are in turn modelled computationally using molecular dynamics, allowing better understanding of the atomic-scale processes controlling friction and wear. Since the last report, we focused on the behavior of silicon-silicon, silicon-diamond, and diamond-like-carbon (DLC)-diamond interfaces. For silicon-silicon interfaces, we found that nanocontacts showed a sliding-history and stress-dependent adhesion, where sliding increased adhesion by more than 16 times, and this effect was enhanced by the applied normal stress. We explain this in terms of stress-activated covalent bond breaking that only occurs during sliding. For silicon in sliding contact with diamond, we observe that the observed adhesion increases with applied stress and speed, and explain this dependence in terms of tip geometry changes due to atomic-scale plasticity. For DLC, we characterized wear during sliding, and the evolution of adhesion forces. Wear was measured as a function of load and sliding distance. Gradual wear with sliding was observed with the wear rate increasing with the average contact stress, but not following the classic Archard's wear law nor to recently observed behavior following transition state theory. The wear behavior over the full range of stresses is well described by multi-bond wear model that exhibits a change from Archard-like behavior at high stresses to a transition state theory description at lower stresses. We then observed that adhesion showed large scatter, which we attribute to stochastic covalent bond breaking and formation events. In summary, this work shows that understanding adhesion and wear requires careful consideration of the interplay of mechanics and chemistry at the interface.

1 Introduction

Our goal is to characterize and understand the atomic-scale mechanisms governing the tribological behavior (friction and wear) of hard carbon materials during initial sliding contact, in order to understand what controls and enables the transition from high to low friction and wear. Developing this scientific insight is important to enable widespread usage of these materials to applications such as vibrating joints[1,2], contacting and sliding surfaces in micro- and nanoelectromechanical systems for sensors and actuators[3], joints in vacuum or anhydrous environments (as found in the **upper atmosphere and in outer space),** and protective coatings for bearings, bushings, and gears in engines[4,5], turbines[6,7], and other aerospace components. The research was carried out using a unique *in situ* transmission electron microscopy (TEM) nanotribometry method that both PI's have collaboratively developed, thanks in part to prior AOARD support. This method allows us to visualize and quantify atomic-level processes occurring in sliding contacts through real time, real space, high resolution TEM measurements of a contact pair, where contact forces are precisely measured and controlled.

DISTRIBUTION A: Approved for public release; distribution unlimited

1.1 Current Challenges in Tribology of Carbon-Based Materials

The mechanical and tribological properties of carbon-based films are, under the right conditions, superior to almost all other materials. Diamond, the stiffest and hardest bulk material known, can be grown in a smooth nanocrystalline thin film form with equivalent mechanical performance (ultrananocrystalline diamond - UNCD). These films can exhibit friction coefficients of 0.01 and less (as slippery as ice), and wear rates corresponding to fractions of an atomic layer per pass of the sliding interface ($<10^{-10}$ $mm^3N^{-1}m^{-1}$) with no lubricant needed [8-10]. These characteristics far exceed those of well-lubricated interfaces of high performance steels and other expensive coatings.

Despite this potential, the widespread use of these materials is inhibited by a lack of scientific understanding of the initial process of wear, the so-called "run-in" process. While the steady-state wear rate and friction is often low, the *initial* rate of friction and wear during the "run-in" period, can be high. This "run-in" period may consist of only a few cycles of sliding, during which the contacting asperities become smoother, and local stresses, friction, and wear decrease, sometimes by *orders of magnitude*. However, in some cases, this "run-in" continues indefinitely [11-14]. This is a catastrophic outcome: sliding parts can wear out far earlier than expected, or seize. Small changes in load, environment, sliding rate, surface roughness, and sample preparation have been observed to affect whether or not this crucial transition takes place. Results are largely empirical; there is a lack of scientific understanding of the atomic-scale processes in the contact that control whether the transition to low friction and wear occurs. Developing fundamental knowledge of these processes is crucial, and is the key to rationally designing and controlling coatings and operating parameters so that stable, low, reliable friction and wear performance can be obtained for engineered systems using these materials.

Previous studies by the PIs on interfacial contact conditions including atomic and macro scale studies show that the behavior of individual asperity contacts at the nanoscale plays a critical role in the run-in process[15-19]. More recent research, including by the both PI's, points toward specific atomic-scale mechanisms strongly affecting the sliding behavior of these materials, including: rehybridization from sp^3 to sp^2-bonding of the C atoms[20], formation of bonds across the interface and subsequent atomic bond breaking[21], and the strong passivating influence of small quantities of adsorbates[9,22]. However, many of these observations are indirect or inferred, and others have not been studied in a systematic way that allows understanding of the run-in transition (namely the contact interactions on the surface separation and the real contact area for an asperity) to be investigated.

2 Experimental methodology

2.1 *In situ* TEM Tribometry

To address our research goals, over the last few years we have developed a unique *in situ* TEM tribometry method that allows atomic-scale characterization of a single-asperity sliding contact. Both PI's Carpick and Jeng have a Hysitron PI-95 PicoIndenter TEM specimen holder, which was used for this purpose. This instrument measures normal load and displacement simultaneously inside a TEM, and can position an indenter in three dimensions with nanometer scale precision (Figure 1). While the standard configuration is designed for indentation, we developed a method for laterally sliding the indenter (by using integrated piezoelectric controls) against an atomic force microscope (AFM) cantilever. In this configuration, we can study the sliding behavior of several contact pairs (one material in the indenter, other material in the AFM tip) while observing the process with the TEM, allowing atomic-scale resolution of the mechanisms of deformation, adhesion, friction, wear, and failure at the sliding interface.

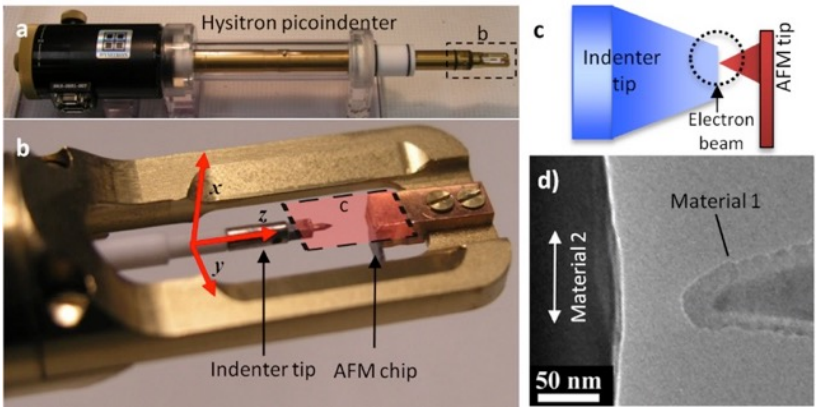

Figure 1: *In situ* TEM setup. (a) The Picoindenter TEM holder. The dashed rectangle is shown in b) in more detail. A piezo tube allows the indenter to attain three dimensional motion with sub-nm resolution.

(c) Schematic close up of the AFM cantilever and indenter tip. (d) TEM micrograph of a typical experiment, where characterization of the sliding contact between the material of the AFM tip (#1) and the material of the indenter (#2) can be visualized with high resolution

The *in situ* TEM methodology has the key advantages of live-imaging the process of wear and of resolving volumes removed from the sliding asperity as low as 25 nm^3 in volume[23]. These capabilities are critical for probing the run-in period of wear. Moreover, since the measurements are carried out *in situ*, the analytical and crystal-characterization capabilities of the TEM can be leveraged to obtain further insights on the wear processes. All these can be done in sequence with sliding experiments to observe and understand the structural changes occurring.

As part of the present project, the PI developed and published a method for enabling characterization of AFM cantilever probes in the AFM[24]. While scanning probe microscopy (SPM) enables detailed characterization of the geometric, mechanical, and transport properties of surfaces, the technique is often hindered by incomplete knowledge of the shape of the scanning probe. Various authors have measured tip geometry using scanning of known features or imaging of the tip using electron microscopy. The former technique requires complex numerical algorithms with multiple analysis parameters; the latter typically requires custom fixturing and suffers concerns about repeatability and contamination. Here we demonstrate a novel fixture and a practical guide to imaging SPM probes using electron microscopy, which minimizes or eliminates these disadvantages. The dissemination of this fixture and technique will enable a broader community of researchers to improve the quality of SPM imaging and the quantitative analysis of results.

The experimental procedure consists of bringing the indenter surface and AFM tip in contact; the force is controlled by displacing the indenter beyond this point a given amount against the AFM tip, whose spring constant has been calibrated before. Subsequently, lateral sliding motion at a predetermined speed and duration is imposed on the contact. After sliding is finished, the contact is separated. This process is captured on video, allowing post-processing analysis for metrology of the force and observation of failure events. Furthermore, before and after sliding, high-resolution images of the tip are recorded, thus allowing visualization of volume loss (wear) due to sliding (quantified in post-processing), and of any structural change.

2.2 *In situ* TEM Nanoindentation Experimental methodology: tip on tip and tip on flat

The experimental methodology using the followed here is identical to the methodology in Ref. [1] except where an AFM tip was used as the lower surface in place of a diamond indenter. The following gives a detailed account of the methodology.

The upper AFM cantilever spring constants in these experiments were calibrated with the Sader method[2]. The spring constants ranged from 0.20 to 1.51 N/m. The experimental steps were:

1) obtain images of the upper AFM probe at a range of magnifications; magnifications from 40kx to 80kx are optimal for subsequent comparison to tip images after sliding since they include features from the sides of the tips (the shank), which provide stable fiducial markers to align images before and after each sliding test,

2) align the upper silicon probe in the focal plane of the lower diamond indenter or silicon probe,

3) slowly (<1 nm/s) bring the lower probe or indenter toward the upper silicon probe using fine z-positioning whereupon a snap-in of the cantilever and probe occurs when the gradient of the probe-sample interaction force (primarily due to van der Waals (vdW) attraction) exceeds the spring constant of the cantilever,

4) execute sliding if desired,

5) halt sliding and slowly (<13 nm/s) manually retract the diamond indenter or lower silicon probe to break contact; adhesion will keep the upper probe in contact with the indenter or lower probe until the spring force from the upper cantilever exceeds the adhesive force, at which point the upper probe quickly snaps off of the indenter's surface, and

6) obtain images of the upper probe at similar or identical magnifications and conditions as the pre-test images from step 1.

3 Results and Discussion

3.1 Silicon adhesion probed with the *in situ* TEM nanoindentation methodology

Silicon is the most abundant element in terrestrial rock, it is the primary material used in the semiconductor industry, and is the primary material used in scanning-probe microscopy (SPM or AFM) and tip-based nanolithography (TBN) research and industries. Thus, a complete understanding of its surface properties and interactions with other materials of interest is of general importance. Using our unique *in situ* TEM

nanoindentation and sliding methodology, we discovered never before observed adhesion phenomena experienced by self-mated silicon contacts and silicon against diamond. Though adhesion generally increases with sliding speed and stress regardless of the material pair, there are clear differences between them in the mechanisms controlling adhesion.

3.1.1 Self-mated silicon nanoasperities show sliding-history and stress-dependent adhesion

Six groups *in situ* TEM tip-on-tip nanoindentation and sliding experiments were done on six different days with different self-mated silicon probe systems. The native silicon dioxide was removed by either wearing it off prior to recording data or by fracturing the apexes of each probe before acquiring data. Figure 2 provides details for the history of each probe system. Tests done within a group were either contact-separate (CS) or contact-slide-separate (CSS). As their names indicate, CS tests had no sliding whereas sliding was induced after coming into contact during CSS experiments.

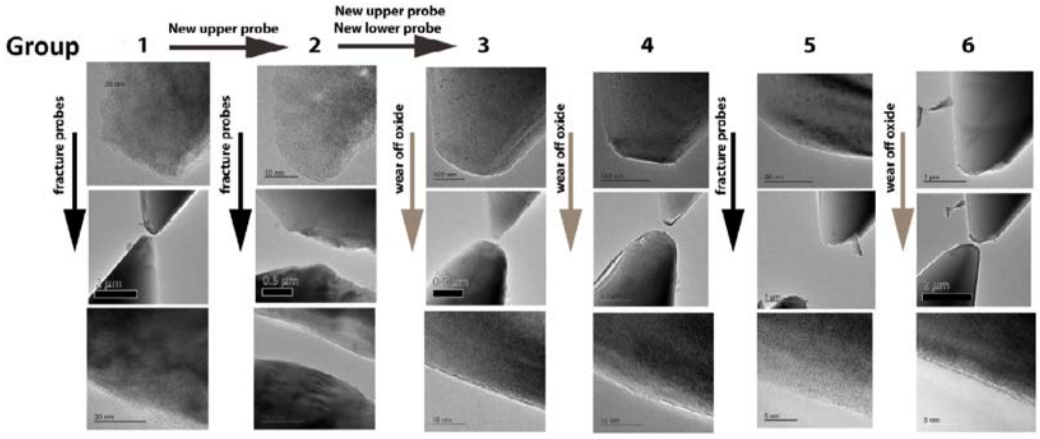

Figure 2 Images of the probes used in the six groups of experiments (columns labeled by experiment number) taken before all experiments in that group (first row), during a representative experiment in that group (middle row), and after a representative experiment in that group (bottom row). Down arrows indicate whether the oxide was removed via wear or fracture and right arrows indicate when a different probe from the previous probe was used.

Over two hours of video consisting of 433 CS and CSS experiments was captured and is available at this link https://youtu.be/CE1ROm_rmXg

The videos clearly show that adhesion is very low when performing a CS experiment, but it surprisingly increases substantially when sliding is induced during a CSS experiment. Furthermore, when a CS experiment is performed immediately following a CSS experiment the adhesion usually returns to low or undetectable values. This is the first observation of reversible i.e., sliding-history-dependent adhesion for any material and certainly the first observed *in situ*. This phenomenon has important implications for tunable adhesion technologies like transfer printing and pick-an-place manufacturing where the ability to control the magnitude of adhesion is critical.

Statistics of the adhesion force are shown in Figure 3 and are differentiated by group, demonstrating the significant statistical increase of adhesion that occurs when sliding is induced. Overall, there was an average of 19 times increase in adhesion from CSS tests over CS tests and increases as high as 32 times were measured.

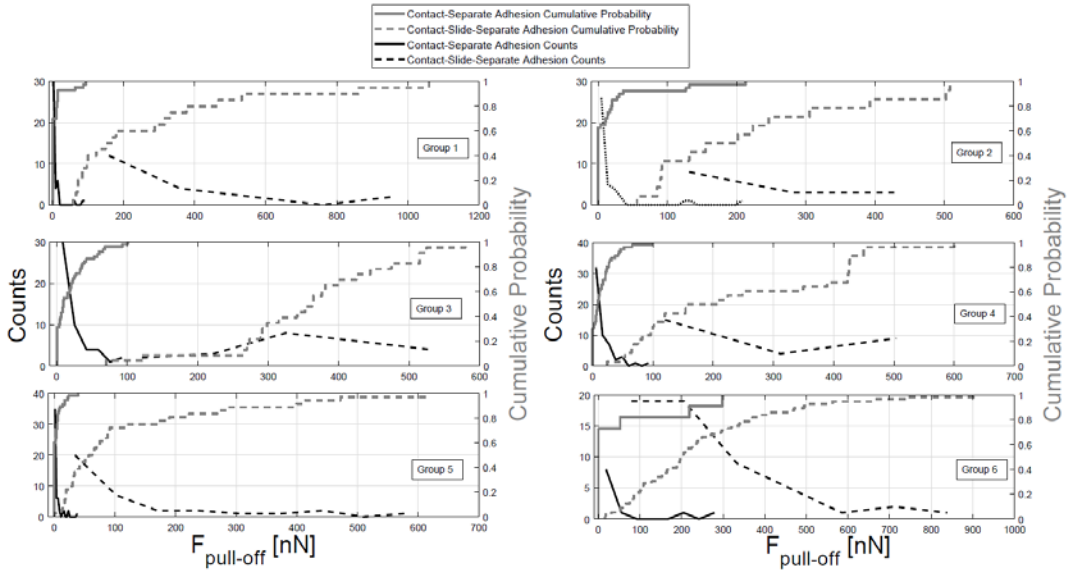

Figure 3 Statistics for the adhesion experiments. Shown are the cumulative probability of the pull-off forces (gray solid and dashed lines, right axes) versus pull-off forces and the counts (black solid and dashed lines, left axes) of the pull-off forces versus pull-off force, all demarcated by whether sliding was induced. The number of bins was calculated using the Freedman-Diaconis rule to more closely resemble the underlying distribution.

It was also observed that the rate of increase of adhesion with sliding speed was influenced by contact stress, which itself was estimated using the DMT contact mechanics approximation for normal stress of hard spheres with short-range adhesion. This dependence is shown in Figure 4 and grows quite linearly with the stress.

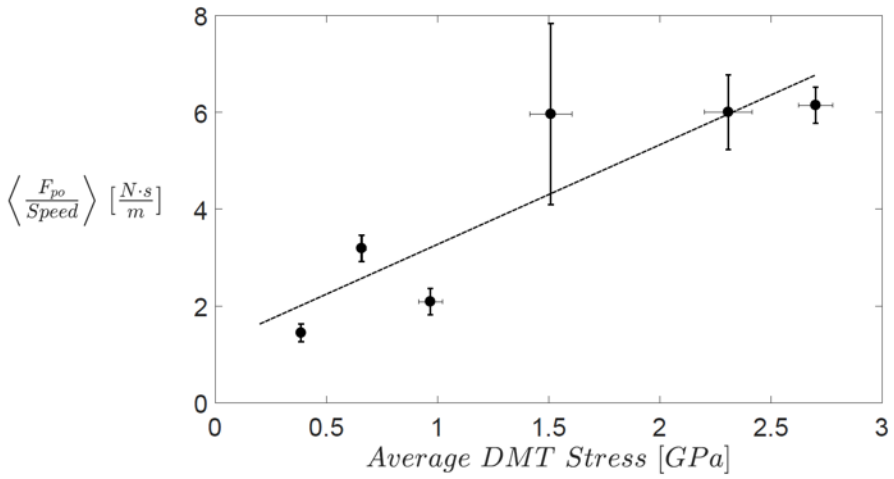

Figure 4 Average $\left\langle \frac{F_{pull-off}}{speed} \right\rangle$ vs. average DMT stress for all contact-separate and contact-slide-separate tests. The dashed line is a linear fit. The error bars are standard deviations of the means.

We hypothesize that the reversible and stress-dependent nature of adhesion can be explained by the stress-modulated evolution of silicon surface passivation, as detailed in Figure 5. Initially, the silicon surfaces exposed to the TEM chamber after removing their oxide will be highly reactive and residual molecular hydrogen within the chamber will form silicon-monohydride bonds. These are low energy and thus highly unlikely to form bonds, which is why low adhesion is measured during CS tests. However, when sliding is induced, the high shear stress that arises from the speed dependence of friction vis-à-vis the thermal Prandtl-Tomlinson (PTT) model [3–7] will break the monohydride bonds and re-expose reactive silicon atoms, which can form covalent bonds across the interface, thus significantly increasing adhesion. Once the contact is separated, hydrogen repassivates the reactive surface, thus returning the surface to a low-energy state. The work of adhesion measured from CS tests was found to be $8.7 \pm 13.6 \frac{mJ}{m^2}$, consistent with vdW interaction, while for CSS tests it

was found to be $145.5 \pm 92.7 \frac{mJ}{m^2}$ far greater than any previously reported values for any silicon termination and approaching the cleavage energy of Si(111).

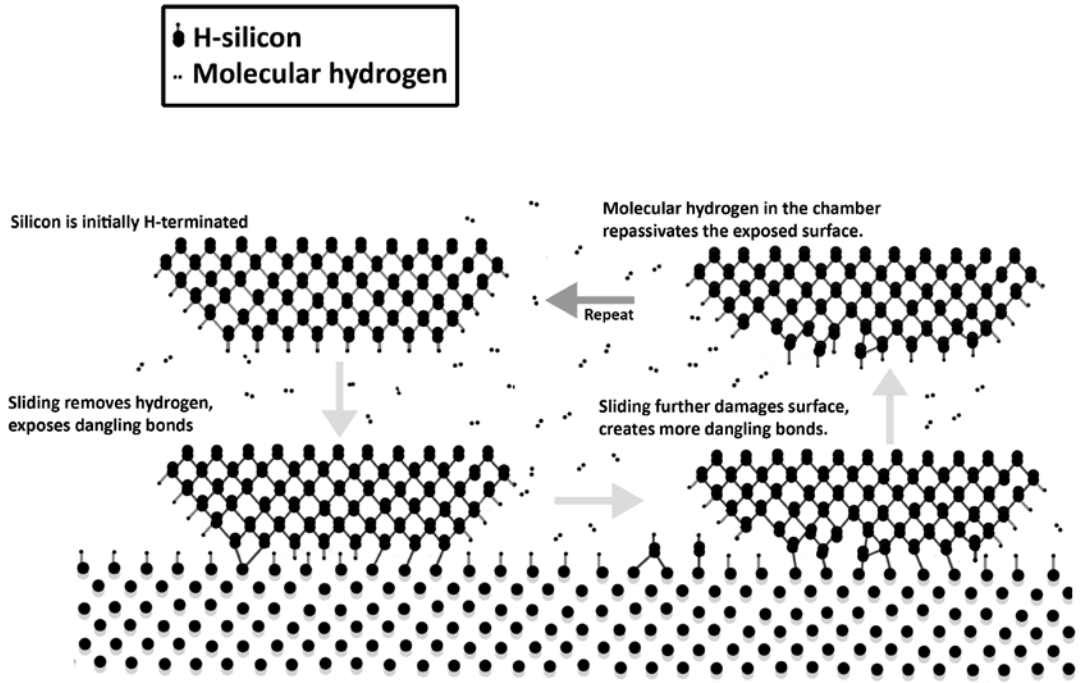

Figure 5 Illustration of the silicon-silicon adhesion mechanism.

A manuscript of this work has been submitted to Nature Materials (NM18072522) and is currently under review.

3.2 Silicon adhesion against diamond as a function of stress and speed

Diamond is the hardest known material and as such is an important surface to study in order to further develop applications where scratch and wear resistance is crucial such as hard-disk drive coatings and cutting tools. Diamond is also being looked at as a potential replacement for silicon in semiconductors and MEMS; diamond has a larger bandgap than silicon, is a better conductor of heat, and has superior electron mobility. Having a deeper understanding of diamond's surface properties and tribological mechanisms will be very useful for future commercialization. In this work, we performed *in situ* TEM nanoindentation of silicon nanoasperities sliding against flat diamond surfaces.

We found that adhesion of silicon sliding against diamond depends strongly on both contact stress and sliding speed. Molecular dynamics (MD) simulations performed by our collaborators of varying silicon probe roughness, diamond surface chemistry, and contact/sliding conditions complement the experimental studies. These coupled studies contribute to the growing body of adhesion research that is revealing the role of controlled energetic inputs such as temperature and normal and shear stress on interfacial chemical behavior.

3.2.1 Silicon asperities sliding against diamond show sliding-speed and stress-dependent adhesion

A fundamental mathematical description of the experimentally measured pull-off force of a spherical silicon tip on a flat diamond surface yields

$$F_{eff} = F_{vdW} + F_{BOND} + F_{SUPP} \quad (1)$$

where F_{eff} is the experimentally measured pull-off force. For a spherical tip against a flat surface, this effective force is a combination of several contributions. First is the van der Waals force of an ideal sphere against an ideal flat surface in the DMT approximation i.e., $F_{vdW} = \frac{W_{vdW}}{2\pi R}$, where W_{vdW} is the van der Waals work of adhesion and R is the radius of the sphere. Next is the force to cleave any bonds, F_{BOND}. Finally, any supplemental forces that arise either due to deviations from the ideal geometric assumptions arising from roughness can be condensed into one term, F_{SUPP}. Thus, the effective work of adhesion between a spherical tip

and a surface can be defined as

$$W_{eff} \equiv \frac{F_{eff}}{2\pi R} = W_{vdW} + \frac{F_{BOND}}{2\pi R} + \frac{F_{SUPP}}{2\pi R} \quad (2)$$

The effective work of adhesion for these tests W_{eff}, as defined in equation 2, is plotted against the normal contact stress in Figure 2. The normal contact stress σ_N, was calculated using the DMT model [18]. All tests were conducted at adhesion only i.e., with no external applied force.

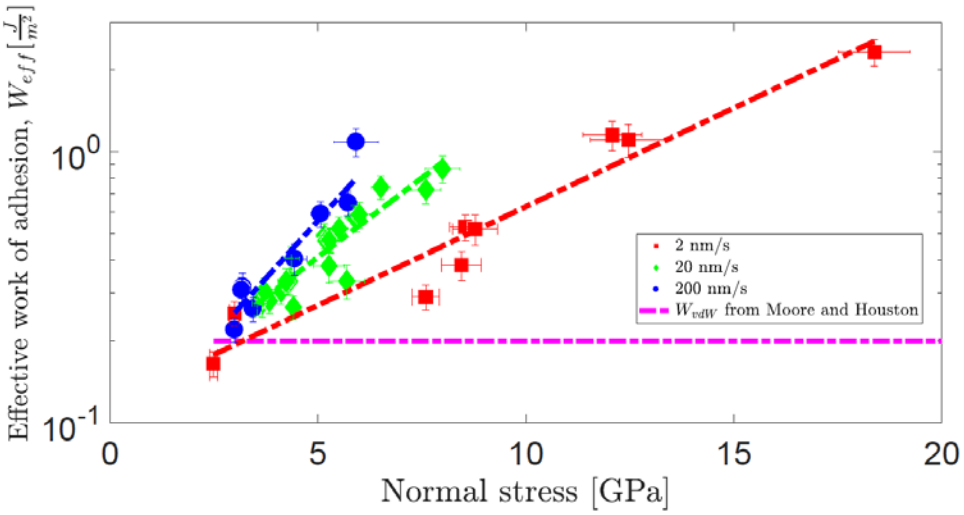

Figure 6 Effective work of adhesion plotted against the DMT normal contact stress for the speeds 2, 20, and 200 nm/s. The magenta line is an estimate of the ideal work of adhesion for silicon against diamond taken from Moore and Houston [8].

Remarkably, W_{eff} increases exponentially with normal stress. W_{eff} *also* increases with sliding speed for a given normal stress. Figure 7 illustrates the growth of exponential coefficient b from a fit to the heuristic equation $W_{eff} = a\,exp\,(b \times \sigma_N)$ on sliding speed, exhibiting the logarithmic trend.

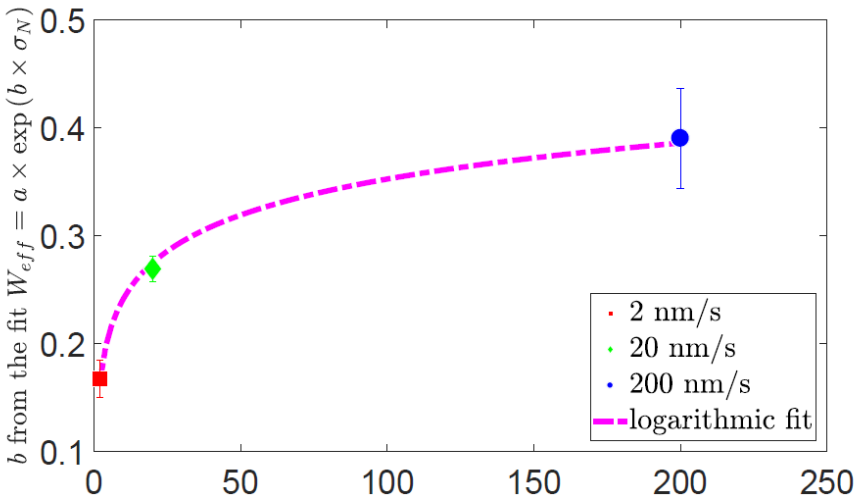

Figure 7 The slope from Figure 2 for each sliding speed, showing that the adhesion grows logarithmically with sliding speed

Simulations provide unique insights into the complex phenomena occurring in the interface between silicon and diamond. For this study, simulations with varying diamond hydrogen termination, applied force, silicon tip roughness, and sliding speed were performed. Figure 8 shows three time-sequential snapshots of a simulation of a rough silicon tip sliding on 100% Hydrogen-terminated diamond. It shows that the initially rough surface is smoothed out through plasticity and wear.

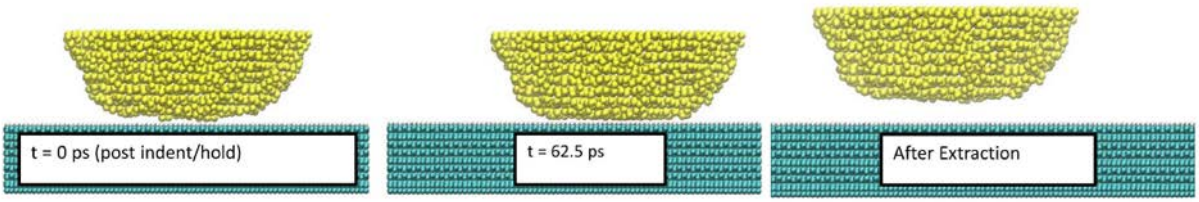

Figure 8 Sequential video snapshots from a simulation of a rough silicon asperity sliding against 100% H-terminated diamond. The roughness of the apex shown in the first frames is reduced during sliding and is apparent after contact is broken.

Relative to indent-only tests, the mechanism of smoothing during sliding tests increases adhesion. This is shown quantitatively in Figure 9 which displays force-distance curves for (a) indent-hold retract (IHR) tests and (b) indent-hold-slide-hold-retract (IHSHR) tests i.e., tests with sliding, for different applied forces. For IHR and IHSHR tests adhesion, which is the most negative normal force value, increases in magnitude when applied force increases. This is due to wearless and atomic-level plastic deformation due to irreversible compressing of protruding atomic asperities. Thus, we have identified one possible mechanism that modulates $\overline{F_{slipp}}$: stress and sliding-induced smoothing of the tip surface. This modulation likely only has an effect on the lower values of $\overline{W_{eff}}$. Importantly, the true $\overline{W_{adh}}$ i.e., $\overline{W_{mdw}}$, must then lie somewhere between the lowest value reported in Figure 6 and the highest, with all changes of $\overline{W_{eff}}$ smaller than $\overline{W_{mdw}}$ with stress and speed occurring because of smoothing and changes in $\overline{W_{eff}}$ larger than $\overline{W_{mdw}}$ with stress and speed being dominated by stress-activated covalent bonding.

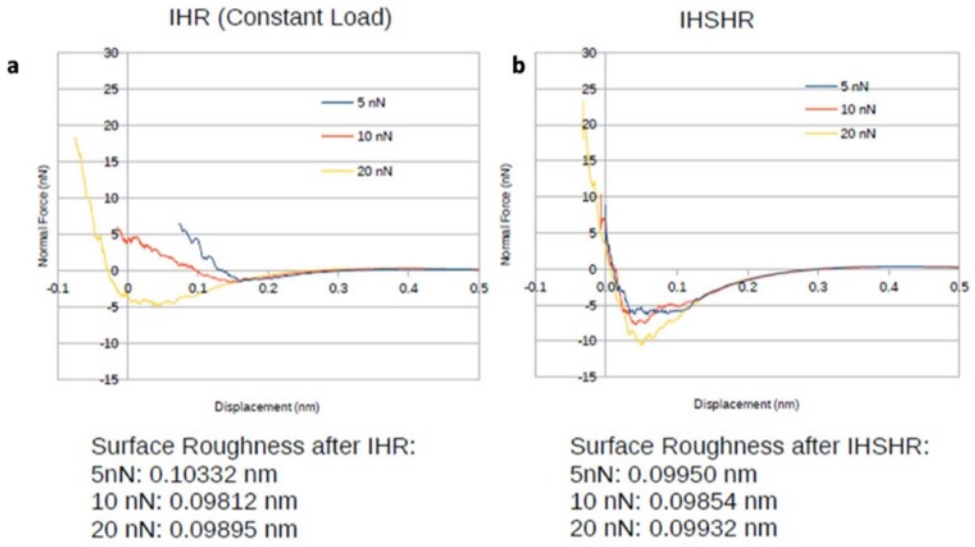

Figure 9 Force-displacement curves during retraction only for a rough silicon tip against 100% hydrogen terminated diamond from MD simulations for (a) indent-hold-retract and (b) indent-hold-slide-retract. Adhesion is greater in the case of sliding and also increases with increased applied force. Text below each graph indicates roughness values. Roughness does not change substantially from indenting or sliding.

A manuscript detailing this work is in preparation.

3.3 DLC wear and adhesion and the extended Multi Bond (eMB) wear model

Diamond-like carbon (DLC) has exceptional mechanical and tribological properties such as high hardness, low wear (in humid environments), and low friction. DLC is thus a material that is of great interest in several industrial and research applications such as hard disk drive coatings, cutting tool coatings, low friction surfaces, scanning-probe microscope coatings, and aerospace applications. For the latter application, it is necessary to properly quantify DLCs properties under a range of environmental conditions, but one very important environment is vacuum since space is a vacuum. Additionally, studies in vacuum eliminate the environmental variable such that results for a material pair are fundamental.

The wear and adhesion behavior of DLC asperities in vacuum has not been previously explored to the extent that silicon, another important material, has enjoyed. Nor has there been a concerted effort to compare wear behavior of DLC nanoasperities between environments. To fill in these gaps in knowledge we performed both *in situ* TEM wear and adhesion experiments in vacuum and *ex situ* AFM wear experiments in an environment with a small level humidity. To gain a better understanding of the adhesion results we collaborated with experts in molecular dynamics simulations at the United States Naval Academy and Oakland University. The wear results were analyzed with a new wear model developed in collaboration with researchers at Johns Hopkins University.

3.3.1 *ex situ* DLC AFM wear and extended Multi Bond (eMB) wear model

Seven DLC-coated AFM probes were worn at varying applied forces against Nioprobe surfaces in a controlled relative humidity of 3 ± 3%. The probes were imaged in TEM before wear, after specified intervals of wear against the Nioprobe surfaces, and after completion of the wear tests. Figure 10 shows TEM images of the seven probes used in this study before sliding, after 102 mm of sliding and after 512 mm of sliding. Progressive wear of the DLC coating is readily apparent and its severity correlates strongly with applied force, F_{ext}. Figure 11 shows AFM topography images from scans with the seven probes against Nioprobe surfaces. The gradual dulling of the probes is evident from the decreasing resolution of the sharp features of the Nioprobe surface as the experiments progress. Figure 12 displays traces of the two-dimensional TEM profiles of the seven DLC-coated probes imaged at specified intervals in the wear experiment.

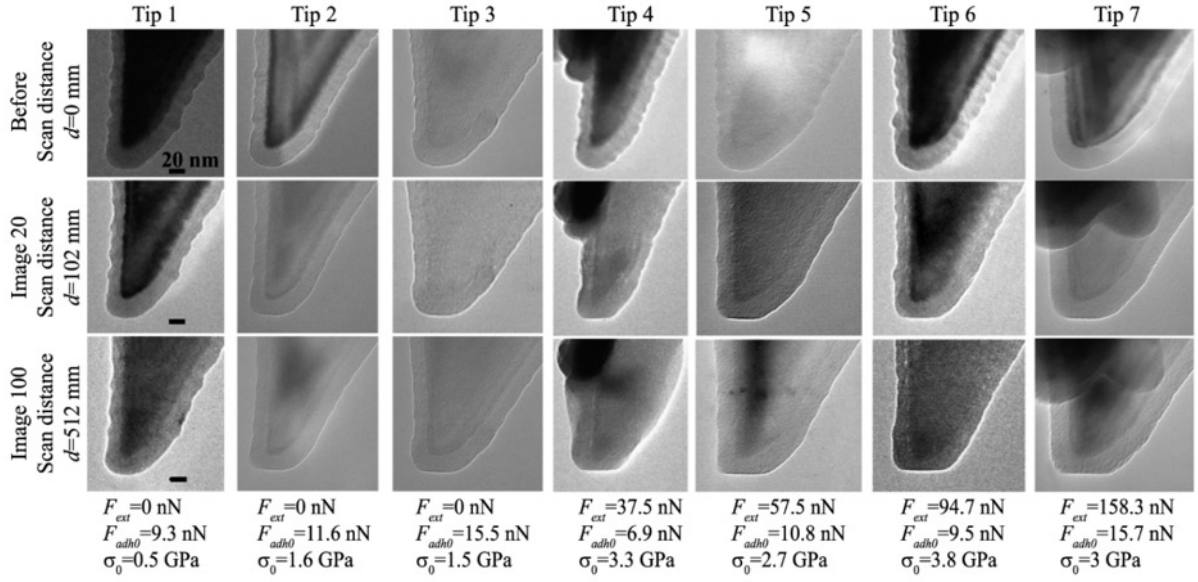

Figure 10 TEM images of the seven DLC-coated Si tips showing the evolution of tip geometry due to wear with sliding. Images of each tip before the wear scans (top row), after sliding for 102 mm (middle row), and after sliding for 512 mm (bottom row). The loading conditions, including the applied external load, F_{ext}, the initial adhesive load, F_{adh0}, and the calculated initial mean contact pressure, σ_0, are listed.

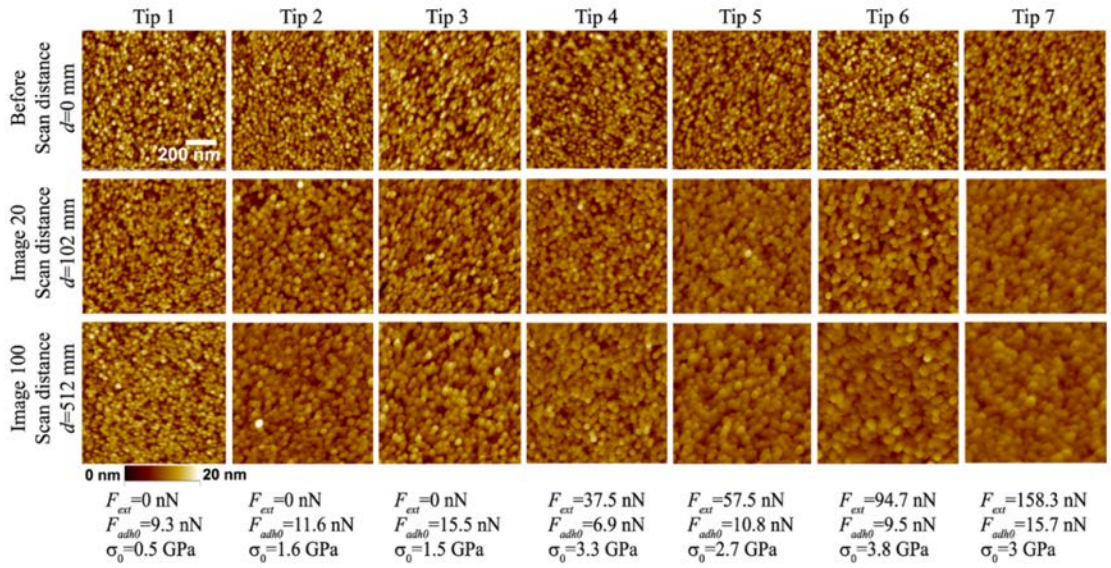

Figure 11 Contact mode topographic AFM images of Nioprobe surfaces acquired using tips 1−7 before the wear test (top row), after scanning 102 mm (middle row), and after scanning for 512 mm (bottom row). The in-plane (x−y) dimensions of the AFM images are 1 × 1 μm^2, and the z-height range of all AFM images is set at 20 nm (see contrast bar).

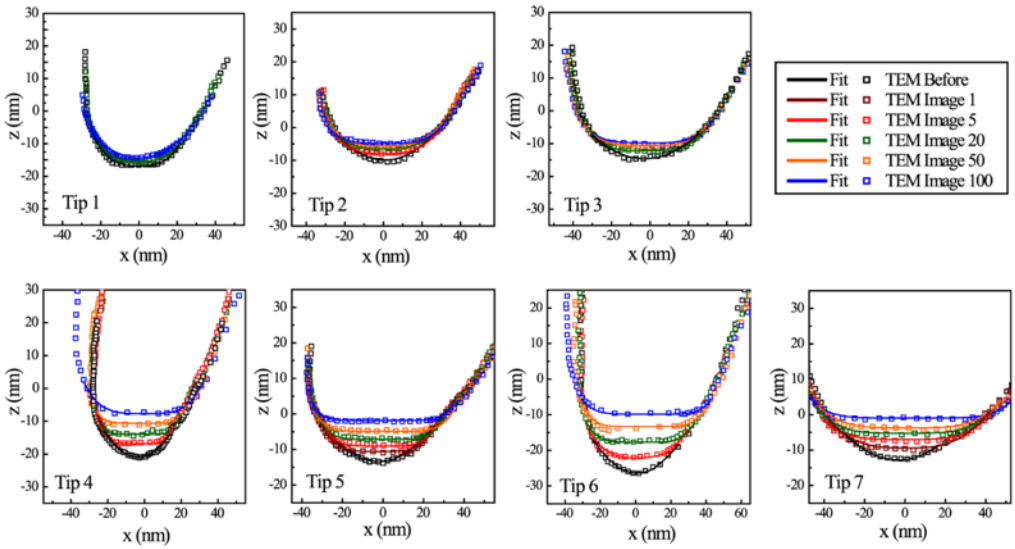

Figure 12 Two-dimensional (2-D) tip profiles extracted from the TEM images of tips at different scan distances. Symbols represent data obtained from image processing of TEM images, whereas solid lines are power-law fits to the tip profiles.

A recent model developed at the University of Pennsylvania describes a new wear process known as atom-by-atom (ABA) wear[1]. As the name suggests, ABA wear is gentle removal of single atoms, as opposed to the more commonly observed abrasive wear seen in macro and mesoscale studies. Using the wear volume obtained by subtracting probe volumes calculated from TEM images taken before and after sliding increments, V, along with DMT contact mechanics estimates of the contact area $Area$ (which uses the probe radius and total normal force), and also the sliding time, t, we estimated the reaction rate $\Gamma_{atom-loss}$ i.e., the rate at which atoms are lost due to wear, normalized by the average number of atoms in contact:

$$\Gamma_{atom-loss} = \frac{V \times \rho_{volume}^{DLC}}{t \times Area \times \rho_{surface}^{DLC}}. \qquad (3)$$

This equation relates directly to Arrhenius kinetics. An equation was proposed to compare the experimental data analyzed with equation 3 to a form consistent with Arrhenius chemical reaction rates i.e.,

$$\Gamma_{atom-loss} = f_0 \exp\left(\frac{-\Delta U + \Delta V_{act}\sigma}{k_B T}\right), \qquad (4)$$

where f_0 is the attempt frequency on the order of 10^{13} to 10^{14} s^{-1}, ΔU is the activation energy to wear an atom, ΔV_{act} is the activation volume, σ is the DMT normal stress, k_B is Boltzmann's constant, and T is the temperature. Figure 13 plots ABA wear results for all seven DLC probes using equation 3 against the DMT normal stress σ. Also plotted is a fit using equation 4, which shows good consistency with data at low stresses but is a poor fit at high stresses. To address this mismatch, a more general model of ABA wear was developed in conjunction with collaborators at Johns Hopkins University.

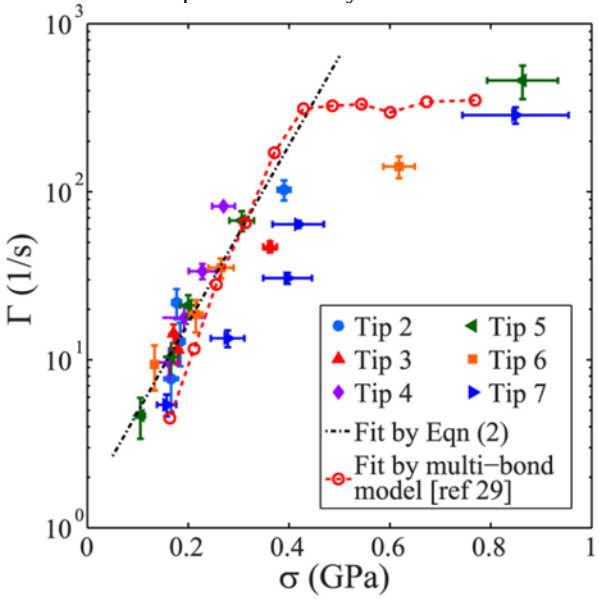

Figure 13 Normalized atomic wear rate (i.e., number of atoms removed from the tip per unit time normalized by the estimated number of atoms in contact) as a function of mean contact stress. Two models are fit to the data: (1) a transition state wear model is fit to data with σ < 0.3 GPa; and (2) a multibond model29 is fit to the full data set.

Figure 14 illustrates the more general kinetics model, which is dubbed the extended Multi Bond (eMB) model. Instead of the wear process being one-way i.e., a bond is formed then worn off, the possibility of the bond breaking without wear is included. In the terms used in Figure 14, an unbonded pair of atoms across the interface must first overcome the energy to bond, denoted as ΔE_{on}. In the low energy state of being bonded it can either wear off by overcoming the energy barrier ΔE_{wear} (a.k.a. ΔU from equation 4) or it can return to its original state by overcoming the energy barrier ΔE_{off}. All of these considerations lead to a more general statement of the reaction rate:

$$\Gamma_{\text{atom-loss}} = -\int_0^{\infty} \left(\frac{\Gamma_{wear}}{\Gamma_{off}+\Gamma_{wear}}\right)\left(\frac{\Gamma_{on}\times\nu}{(\Gamma_{off}+\Gamma_{wear}+\Gamma_{on})\times\Delta x}\right)\left(\frac{dP(\Delta x)}{d\Delta x}\right) d\Delta\lambda \qquad (5).$$

Equation 5 is also plotted in Figure 13 illustrating the eMB model's ability to capture the ABA wear rate at an expanded range of stress where the cruder model of equation 4 cannot.

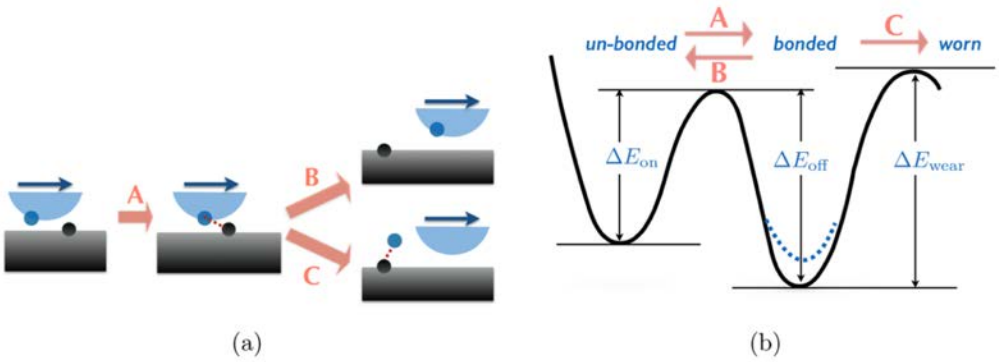

Figure 14 A schematic of the multibond model with wear as an additional process. Transition A represents the formation of bonds between asperity and surface. B represents the breaking of these bonds while C represents the breaking of bonds in the asperity or surface. B represents the breaking of these bonds while C represents the breaking of bonds in the asperity or surface leading to wear.

Manuscripts detailing this work have been published [9,10].

3.3.2 *in situ* TEM DLC adhesion and wear coupled with molecular dynamics (MD) simulations

Using the *in situ* TEM nanoindentation tip on flat methodology, adhesion experiments of DLC probes on a flat diamond indenter were performed. Figure 15 illustrates this experimental setup. Five different tips were used to make and break contact many times in order to accumulate statistics for pull-in and pull-off forces and wear.

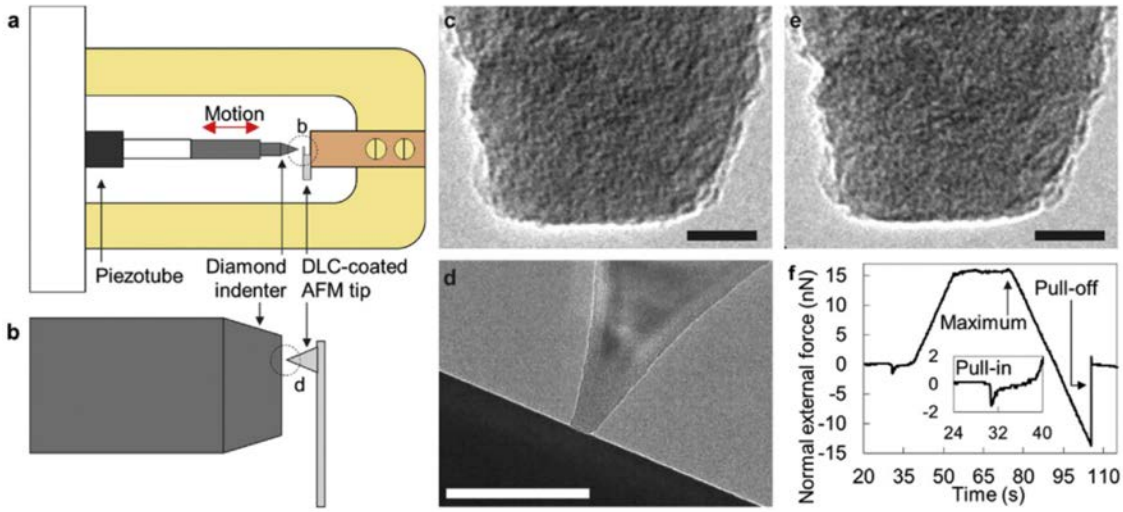

Figure 15 a. Schematic representation of the experimental setup using the Hysitron Picoindenter. The dashed circle is detailed in b, where a schematic close-up of the indenter and AFM cantilever is shown. c. Example of a high-resolution image taken before a contact (scale bar 10 nm). d. Frame of a video during contact (scale bar 200 nm). e. Example of a high- resolution image taken after a contact (scale bar 10 nm). f. Example of a time versus force curve extracted from the TEM videos, showing pull-in force, pull-off force and maximum external force. A close-up of the pull-in event is shown in the inset. d and f were obtained from the same contact event.

Figure 16 shows the evolution of pull-in and pull-off forces across a number of indents from one experiment as well as averages for all experiments. Clearly, the pull-off forces vary more than the pull-in forces. This occurs because pull-in forces are only affected by long-range attractions such as van der Waals (vdW) forces, which are a function only of the geometry, barring material differences. The variability in pull-off forces arises because of covalent interactions that form when in contact. The stochastic nature of bonding leads to large and random pull-off forces.

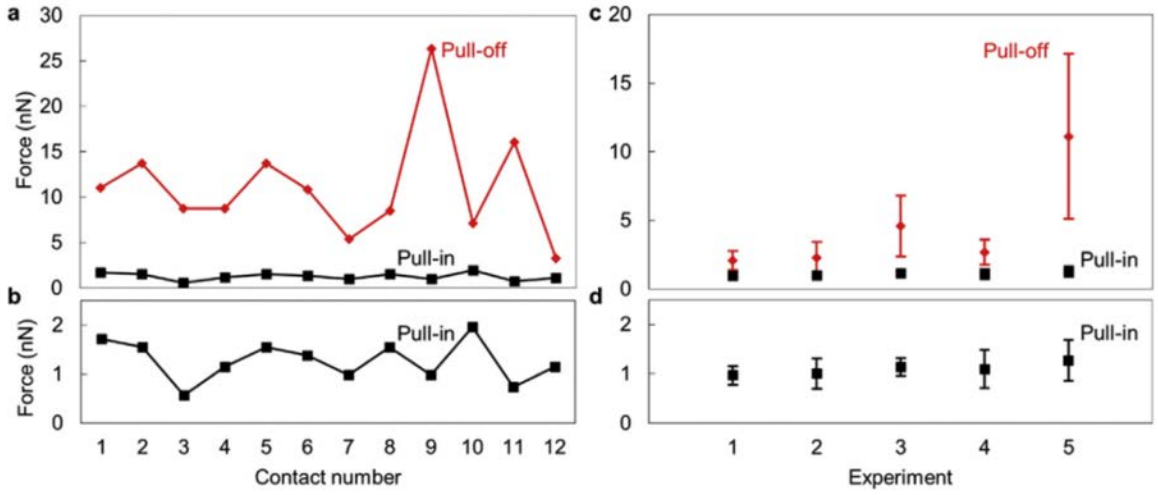

Figure 16 a. Evolution of the pull-in and pull-off forces as a function of consecutive contact number, for one of the experiments. b. Detail of the pull-in forces. c. Mean and standard deviation of pull-in and pull-off forces for all experiments. Experiment 5 corresponds to the data in a and b. d. Detail of the pull-in forces. (A color version of this figure can be viewed online.)

Simulations headed by collaborators at the United States Naval Academy and Oakland University provide further support for the covalent bonding hypothesis. Figure 17 illustrates both the simulated DLC probe and the diamond substrate (darkened areas on the substrate show the different regions where adhesion tests were performed).

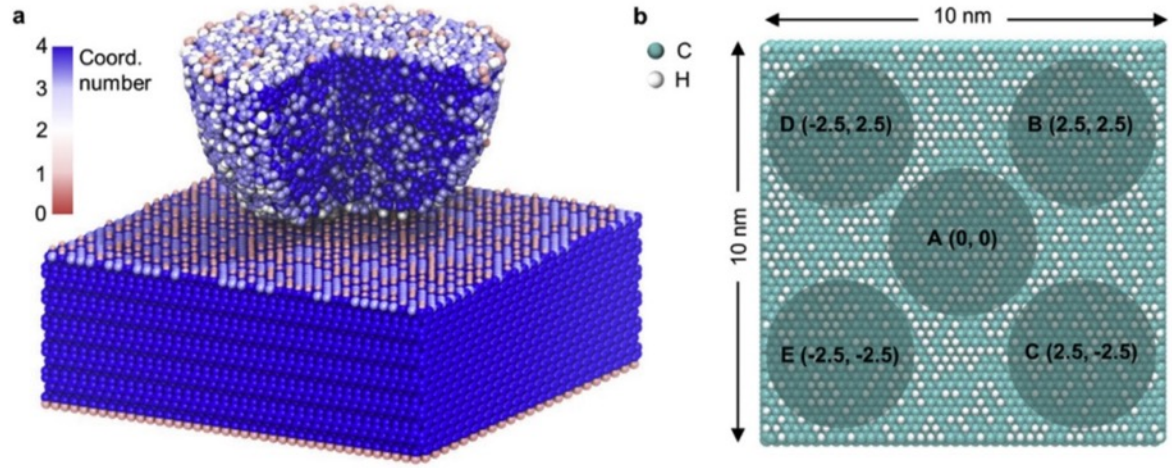

Figure 17 a. Perspective view of the MD simulation setup, with a cross section of the tip to see its internal structure. Small pink spheres represent hydrogen. Carbon atoms are colored by their coordination number. b. Top view of the H-terminated diamond (111) surface. Letters A-E represent different contact points of the tip.

Two different potentials were employed in this study, the AIREBO and the REBO-S. The AIREBO only simulates long-range forces such as vdW interactions and is therefore most appropriate for comparing to pull-in forces. Indeed, as Figure 18 **a** illustrates, pull-in forces (the lowest force in the Force-Distance plot) are very consistent despite the different regions they were measured in. Alternatively, the REBO-S potential models both long-range interactions and covalent interactions and is thus best suited for pull-off forces that are influenced by chemical bonds. As Figure 18 **b** shows, there is substantially more variability in pull-off forces between the different contact regions using the REBO-S potential; this is consistent with there being a stochastic nature to covalent bonding and consistent with what was observed experimentally.

DISTRIBUTION A: Approved for public release; distribution unlimited

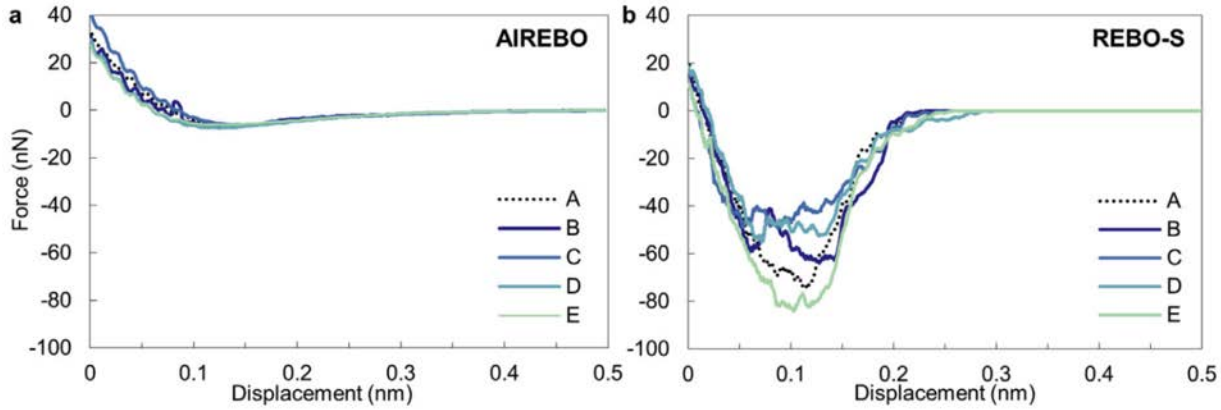

Figure 18 Simulated force versus displacement approach curves obtained using the a. AIREBO and the b. REBO-S potentials. Letters A-E correspond to different contact points on a 40% hydrogen terminated diamond surface.

This collaboration also produced the Hamaker constant of DLC in high vacuum 8.1 ± 9.7 x 10^{19} Joules. An Archard wear rate of 0.001 $mm^3/N.m$ was found consistently between experiments and simulations. This value is significantly higher than values reported for DLC in environment. The wear trends could not be fit by the ABA wear model of equation 4. Analysis is in progress to compare the wear results to the eMB model of equation 5 but it is quite possible that wear of DLC in vacuum (without a passivating environment) is too high to be explained by such a gentle wear regime. Finally, simulations produced results that were quite counterintuitive. Figure 19 shows that, for diamond surface hydrogen termination surface concentrations of 50% and less experience a smaller ratio of pull-off force to number of bonds when sliding is performed, suggesting that lower hydrogen terminations along with the induction of sliding lead to weaker interfacial interactions. This intriguing result is currently being studied closely in collaboration.

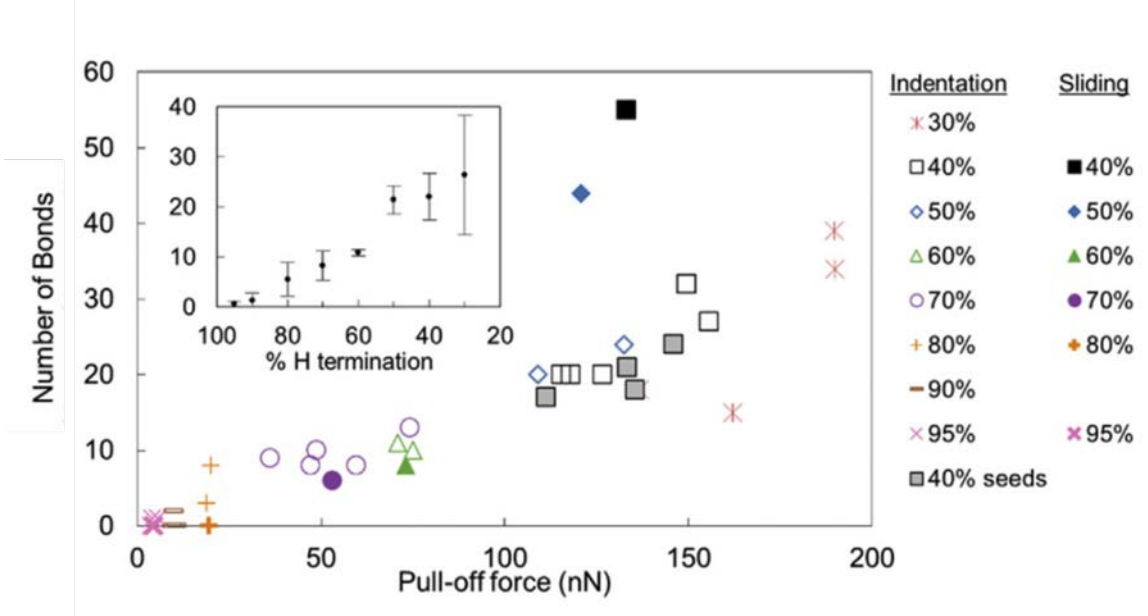

Figure 19 Effect of hydrogen termination on the pull-off force and number of bonds across the interface for both indentation and sliding. Inset summarizes the indentation results.

A manuscript detailing this work has been published [11].

3.4 Multi-scale MD investigations into of Atomic Adhesion-induced Wear

In the theoretical study, an atomic-scale model of mechanical contact behaviors between a DLC tip and a diamond (111) surface has been investigated by PI Prof. Jeng (CCU), in close resemblance to the experiments

(Figure 15). During the initial approach of the DLC tip toward the diamond surface, an attraction (pull-in) occurs due to van der Waals forces between the DLC-diamond interfaces, where subsequently the end of a DLC tip forms a covalent bond across the interface. These bonds attached to the diamond surface are then broken as the DLC tip is retracted, leading to the DLC atoms remain on the diamond surface. The MD simulation results reveal that the adhesion-induced wear between DLC and diamond under ambient conditions (Figure 20), generated by the formation of multiple peel-off mechanism on the asperities of interfaces after the sliding. Atomic-scale adhesion test and MD simulation were used to obtain the relationship between interfacial reactions (pull-in and pull-off behaviors) and physical properties (surface roughness, volume loss and sliding speed), respectively.

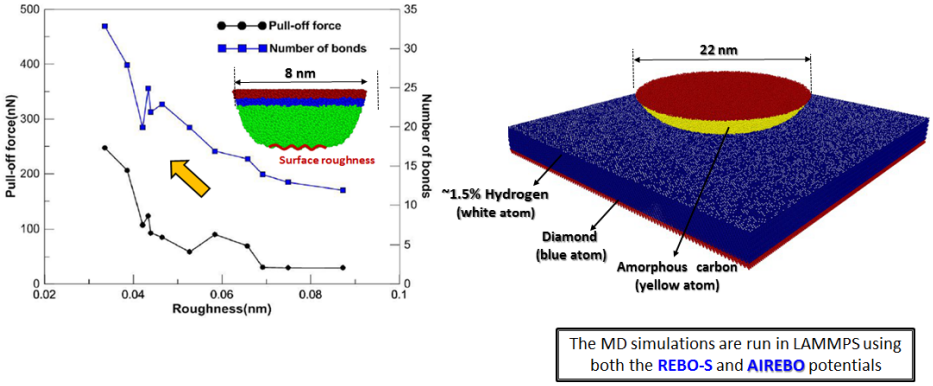

Figure 20 Atomic snapshots showing contact-induced adhesion

3.5 In-situ thermal stability analysis of DLC

A synchronized system integrating Raman spectroscopy and depth-sensing techniques was applied to analyze the microstructure, mechanical properties and surface roughness of DLC films in-situ. This integrated system equipped with a high-temperature chamber coupled with feedback control made it possible to study the temperature effects on the mechanical properties and the microstructure of the films (Figure 21). A series of a-C films with different sp^3 content were deposited on Si substrates using a filtered cathodic arc vacuum (FCVA) deposition system.

Our study confirms previous results that the thermal stability of the a-C films depends on their sp^3 content. The results also show that the structural change is accompanied by a significant increase in the surface roughness. This synchronized characterization technique demonstrates that the film hardness decreases with temperature even before any chemical changes detected using Raman spectroscopy. Moreover, the surface of the films is more sensitive to the temperature compared to the bulk as evidenced by the surface roughness characterization, showing that the surface roughness starts to rise at temperatures lower than for the onset of structural transition in the bulk. Nanoscratch and nanowear further support the conclusion that the surface sensitivity to temperature is greater than for the bulk.

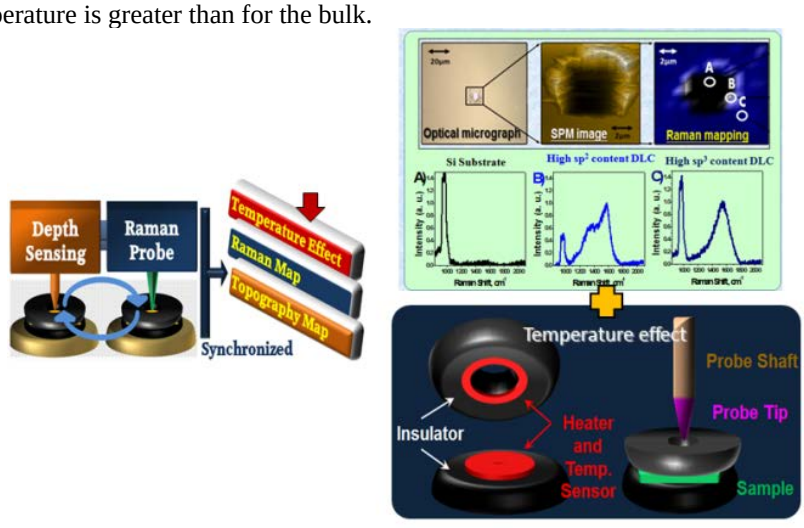

Figure 21 In-situ studies to monitor materials change during the thermo-mechanical tests

3.5.1 As-deposited films structure

To study the effect of the initial sp^3 content of a-C films on their thermal stability, four sample films were deposited under different deposition conditions. The substrate bias voltage and P_{Ar} were varied to change the microstructure of the films. This allowed us to study both the effect of deposition conditions on the microstructure and mechanical properties of deposited films and also their thermal stability. The essential parameters of the deposition are shown in Table 1. Two films 'α' and 'γ' were deposited at similar argon pressure ($P_{Ar}=1.33\times10^{-1}$), but different bias voltage: 'α'– with low bias voltage (-80 V) and 'γ' – with high bias voltage (-700 V). Three films 'β', 'γ' and 'δ' were deposited with similar bias voltage (-700 V), but at different P_{Ar}: 'β' – at $P_{Ar}=0.66\times10^{-1}$, 'γ' – at $P_{Ar}=1.33\times10^{-1}$ and 'δ' – at $P_{Ar}=2\times10^{-1}$.

The Raman spectra of as-deposited films 'α'-'δ' in the range of 900-2000 cm^{-1} are shown in Figure 22(a).The second order Raman peak for Si seen at ~970 cm^{-1} in the spectrum of film 'α' is absent in the spectra of other films. The absence of this peak in the spectra of other films may be due to higher sp^2 contented of these films which should lead to higher absorption coefficient for the Raman probe beam. Trigonally coordinated (sp^2) carbon has a higher absorption cross section for the Raman process [25]. Also, the thickness difference between these films ('β', 'γ', 'δ') and film 'α' should be taken into account (film 'α' is 16 times thinner than the others). The spectrum of film 'α' shows an asymmetric broad peak at ~1550 cm^{-1}, which is the typical visible Raman spectrum of the ta-C films. This asymmetric broad peak could be attributed to the incorporation of the primary G peak and the weaker D peak. The G mode with E_{2g} symmetry involves the in-plane bond-stretching vibration of any pair of sp^2 sites, while the D peak is a breathing mode of A_{1g} symmetry involving only those sp^2 sites in rings. The D mode is forbidden in perfect graphite and only becomes active in the presence of disorder [26].

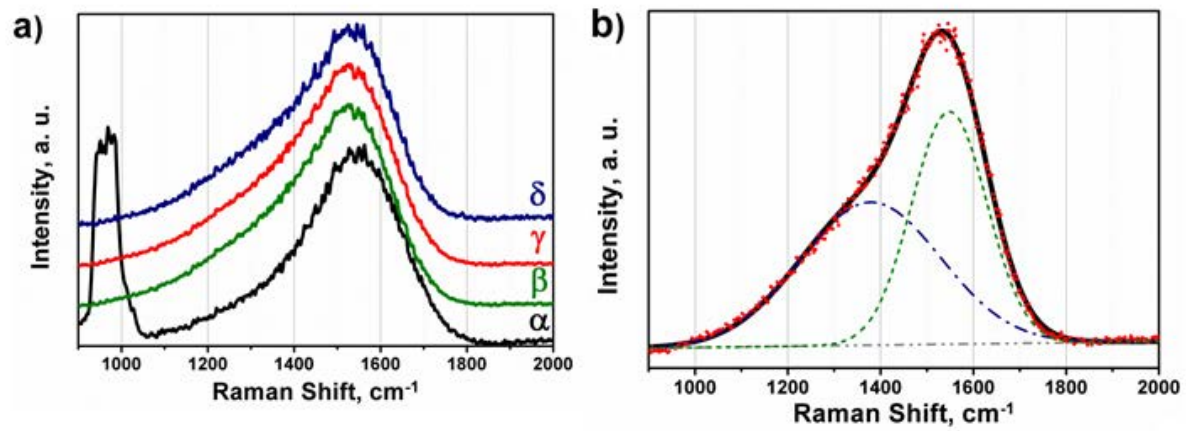

Figure 22 (a) Raman spectra of as deposited films 'α' – 'δ' on Si substrate and b) Gaussian peak fitting of Raman spectrum of as-deposited film 'γ' in the spectral region 900cm^{-1} – 2000 cm^{-1}. The dotted (red) line represents the experimental data for film 'γ', dash-dotted (blue) line shows Gaussian peak associated with breathing vibration of rings (*D* line), dashed line (green) shows Gaussian peak associated with stretching vibration of any pairs of sp^2 sites (*G* line) and solid (black) line shows the fitting envelopes of the Gaussian peaks.

From Figure 22(a) it is obvious that the asymmetric peak is broadening from 'α' to 'δ' and its center is shifting to lower wavenumbers (from ~1550 cm^{-1} for film 'α' to 1530 cm^{-1} for film 'δ'). A multiple Gaussian fit of the spectra into the '*G*'- and '*D*'-peaks enables analysis of the structural differences between these films. Peak fitting was performed in the spectral range 900 – 2000 cm^{-1} using a Gaussian function on the averaged spectrum of the collected spectra (441 spectra) at each temperature. For instance, the result of fitting the spectrum of as-deposited film (at RT) 'γ' is shown in Figure 22(b). It should be noted that the Gaussian function is normally used for disordered materials and the Lorentzian function is expected to give a better fit for less-disordered graphite [26]. In analysis of all spectra, lower fitting error was generally reached using the Gaussian function indicating disorder. Therefore, Gaussian fitting is chosen for this study. However, the fit error of Lorentzian becomes as small as for a Gaussian fit at higher temperatures (T>400℃). This may indicate that the films become more ordered at higher temperatures. Generally, groups using two Gaussians report the area ratio and not the peak height ratios. Although the difference is negligible for disordered graphite, this is not so for a-Cs. For a-Cs, the broadening of the *D* peak is associated with distribution of clusters with different orders and dimensions, while the intensity maximum is correlated to the information about the less distorted aromatic rings [26]. In this paper we refer to I_D/I_G as the ratio of peak heights. The fitting parameter for spectra of as-deposited films 'α' – 'δ' are given in Table 2. The I_D/I_G value shows that the sp^2 content of the films is increasing from film 'α' to 'δ'; hence their sp^3

content is decreasing. This is in agreement with the density value of these films given in Ref.27 [27], as density increases with sp^3 fraction in DLCs.

Although argon injection into the cathodic arc source facilitates the arc discharge (by ionization of Ar atoms), higher P_{Ar} will increase the collision and scattering of Ar ions and atoms with carbon ions and leads to reduction in the energy and flux of carbon ions. Hence, Ar background gas increases the number of ions of low kinetic energy that bombard the growing surface but Ar atoms do not, themselves, participate in the film growth. Therefore, reduction in deposition rate is expected when at the same deposition condition the P_{Ar} is increased [28, 29]. The impact of P_{Ar} on the deposition rate can be found from comparing the deposition rates of films 'β', 'γ' and 'δ' in table I. It is clear that the increasing the P_{Ar} leads to lower deposition rate. At higher P_{Ar} (lower deposition rate), the film growth occurs at reduced carbon ion energy and flux. Therefore, the higher sp^2 content and specific sp^2-bonded configuration is introduced into the film [28-30].

Table 2. Fitting parameters and I_D/I_G values for the Raman spectra of as-deposited films.

Fitting Parameters	Film 'α'	Film 'β'	Film 'γ'	Film 'δ'
G peak centre, cm^{-1}	1558±1	1546±1	1543±1	1539±1
FWHM (*G*), cm^{-1}	218±1	203±1	202±1	190±1
D peak centre, cm^{-1}	1381±1	1392±1	1373±1	1378±1
FWHM (*D*), cm^{-1}	321±1	355±1	357±1	356±1
I_D / I_G	0.32±0.01	0.55±0.01	0.58±0.01	0.61±0.01

It is also expected that film 'α', which is deposited with lower substrate bias voltage (-80 V) has higher sp^3 content than film 'γ', which is deposited at the same P_{Ar} but with higher bias voltage (-700 V). This is because of differences in ion energy at different substrate bias voltages; -700 V will result in much higher ion energies than -80 V. At -700 V just small fraction of the kinetic energy of ions will be used for penetration of ions into the surface and entering subsurface interstitial sites. The rest of their kinetic energy will be released ultimately as phonons (heat). Therefore, there will be a local thermal spike in the growing film at -700 V. This leads to a higher sp^2 fraction for film 'γ' growing at higher bias voltage due to the relaxation phenomena induced by thermal energy. This is in agreement with the Raman spectra of the films 'α' and 'γ' shown in Figure 22 and the higher I_D/I_G value for the spectrum of film 'γ' (0.58) compared to the one for film 'α' (0.32).

3.5.2 High temperature characterizations

- Nanoindenation

Nanoindentation is the most widely used technique for measuring the mechanical properties of thin films. The results of nanoindentation studies on films 'β' – 'δ' are shown in Figure 23. The load-displacement curves were obtained following indentation of the coatings to a maximum load of 3000 μN at different temperatures using a tip specially designed for high temperature studies (with Berkovich geometry indenter). For instance, the load-displacement curves at different temperatures for film 'γ' are shown in Figure 23(a). The gray arrow shows the direction of temperature rise. It can be seen that the maximum penetration depth (h_{max}) increases with temperature rise. The hardness and Young's modulus data of the films 'β' – 'δ' against temperatures are plotted in Figure 23(b) and Figure 23(c), respectively. Unfortunately, we are not able to measure the mechanical properties of film 'α' at elevated temperatures as the tip used for elevated temperature tests is designed with Berkovich geometry which has much flatter tip radius compared to the one used for measuring intrinsic hardness of film 'α' and therefore measured data will be significantly influenced by Si substrate properties for such ultra-thin film. However, the method used to measures the intrinsic hardness of ultrathin film 'α' at RT is described in Supplementary Information. It is obvious that the hardness of the as-deposited films (RT hardness) depends on the P_{Ar} during deposition and increases as P_{Ar} reduces. As explained earlier, at higher P_{Ar} (lower deposition rate) the film growth occurs at reduced carbon ion energy and flux resulting in higher sp^2 content in the growing film. Therefore, one can expect reduction in film hardness by increasing P_{Ar}, as a film with more sp^2 content will show more graphitic characteristics.

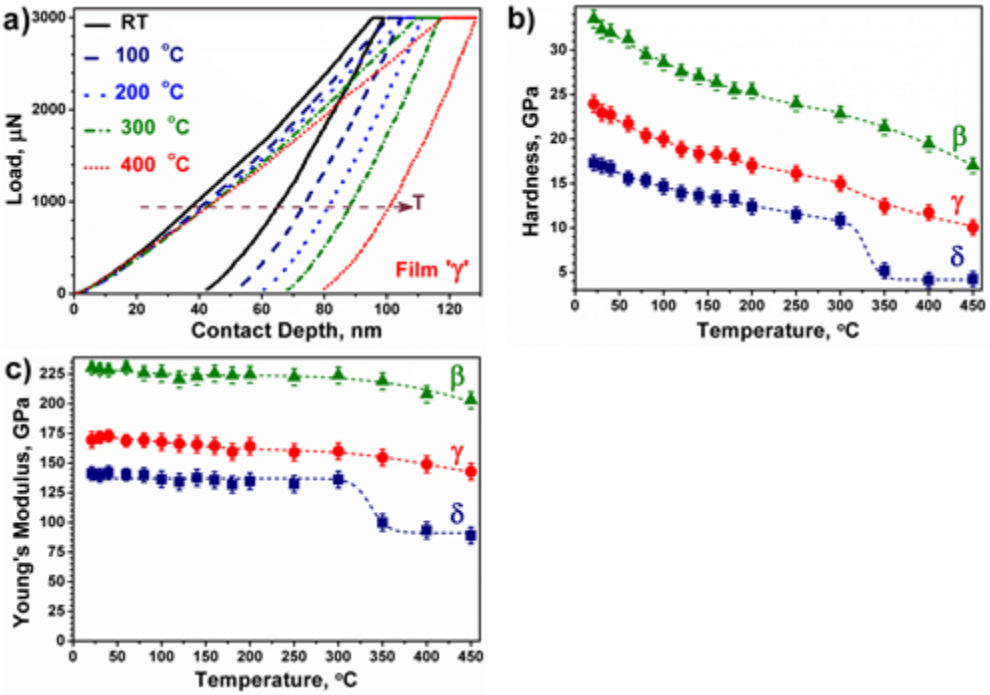

Figure 23 a) The load-displacement curves at different temperatures for a film 'γ' (The gray arrow shows the direction of temperature rise), b) the hardness against temperature and c) The Young's modulus against temperature for films 'β' – 'δ'. Each data is the average of 5 tests. The lines are guide to the eye.

As disused before, the I_D/I_G value for as-deposited films increases from film 'α' to 'δ', indicating ascending order in sp^2 content of the films. This is in agreement with the RT hardness data of the films shown in Figure 23 (the higher the sp^2/sp^3 content, the softer the film). Raising the temperature from RT leads to a slight reduction in hardness of films 'β' – 'δ'. It seems that even small temperature rises affects the hardness of these films. However, the rate of hardness reduction seems to be significantly increased at higher temperatures. For the film 'δ', a sharp reduction in the hardness can clearly be seen when the temperature is raised from 300 to 350℃. Further temperature increase does not change the hardness of this film noticeably. While such a sharp reduction is not clearly evident in the hardness of films 'β' and 'γ', a change in the hardness reduction slope can be detected for these films upon a further temperature increase from 300 and 350℃, respectively. The hardness reduction during early stages of heating may be assigned to relaxation and stress release due to clustering of sp^2 sites in the films [31,32], as it is not expected to have noticeable sp^3 to sp^2 conversion happening at such a low temperatures up to 200℃. Young's modulus of film 'δ' is almost constant with temperature rise until 300℃. after that further temperature rise leads to a sharp reduction in Young's modulus of this film. A similar result can be seen in its hardness (Figure 23(b)). The Young's modulus of films 'β' and 'γ' is constant until 350℃, and after that it starts declining gradually for both films.

- Raman spectroscopy

Microstructure characterization may give more information about the hardness reduction by temperature rise. To monitor probable chemical changes within the films by temperature rise, Raman spectroscopy was used. The Raman spectra of the films over 25x25μm^2 area (21x21 scan points) in the range of 600 – 2400 cm^{-1} were taken at different temperatures and then averaged over the scanned area. The scanned area was kept invariant for each film by temperature rise. The evolution of the normalized Raman spectra of films 'α' – 'δ' by temperature rise are shown in Figure 24(a)-(d) respectively. Every spectrum in Figure 24(a) consists of an asymmetric broad peak at ~1550 cm^{-1} and a square topped peak at ~950 cm^{-1}. The latter is attributed to the second-order Raman spectrum of the Si substrate and decreases with increasing temperature from 350℃, indicating increased optical absorption of the 532nm probe beam by film 'α', presumably from the increased sp^2 content at higher temperature which has a higher absorption cross section for the Raman process [25]. No noticeable change can be seen from the Raman spectra of film 'α' with temperature rise, although, spectra of the other films clearly show evolution of the *D* peak as a result of temperature rise. The *G* and *D* peaks could be seen separately in the spectra of film 'γ' at 450℃ and film 'δ' at 400 and 450℃.

DISTRIBUTION A: Approved for public release; distribution unlimited

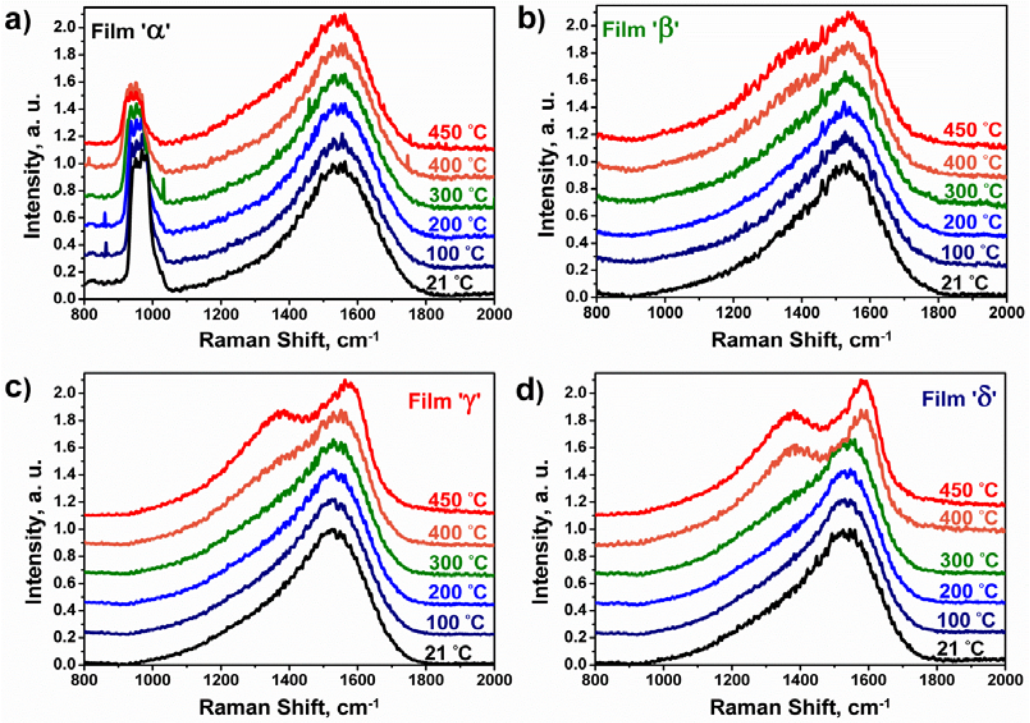

Figure 24. The evolution of normalized Raman spectra of a) film 'α', b) film 'β', c) film 'γ' and d) film 'δ' caused by temperature rise. Each spectrum is the average of 441 scan points.

The I_D/I_G values are plotted against temperature for films 'α' – 'δ' in Figure 25(a). The inserted graph shows the differences in I_D/I_G value of the Raman spectrum at any given temperature and the corresponding I_D/I_G value at RT (Δ I_D/I_G). All films show similar behavior regarding the I_D/I_G change with temperature evolution: with an initial invariant stage and then a rising stage. However, the length of initial invariant stage is different for each film and shortens from film 'α' to 'δ'. This initial invariant stage can be attributed to the microstructure stability of the films. Hence, the thermal stability of the films depends on their initial sp^3 content. For film 'α' the initial invariant stage continues until 400℃, but after that I_D/I_G starts to rise. The rise in I_D/I_G indicates that sp^2-bonded carbon sites are organizing into clusters or ring-like structures [25]. The initial invariant stage continues until 250℃ for film 'β', 200℃ for films 'γ' and 'δ'. Film 'δ' shows different behavior compared to the other films since further temperature rise from 300℃ leads to sharp increase in its I_D/I_G value but after this sharp increase, the I_D/I_G value plateaus at 400℃. Whilst the rate of increase (with respect to T) of I_D/I_G values for films 'β' and 'γ' is much lower compared to film 'δ', as it continues rising until the end of temperature-course for both films.

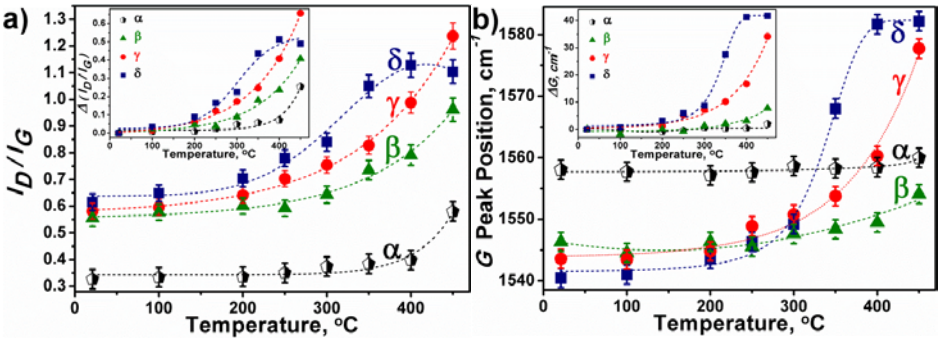

Figure 25. a) The I_D/I_G value and b) G peak position of the Gaussian fits for the spectra of the films 'α' – 'δ' with temperature rise. Each data is the average of tests on 2 samples. The lines are guide to the eye.

Figure 25(b) shows the G peak position in the spectra of films 'α' – 'δ' at different temperatures. The inserted graph shows the differences between the G peak position of the spectrum at any given temperature and the corresponding G peak position of the spectrum at RT (ΔG). Similar to the I_D/I_G changes, the G peak shift with temperature rise has an initial invariant stage and then a shifting stage when it moves to higher wavenumber. However, the shift of G peak for film 'α' which starts with a temperature rise from 400℃ is negligible. The G peak position is almost constant until 250℃ for film 'β', and until 200℃ for films 'γ' and 'δ'. Similarly to the trend in I_D/I_G, an acceding order in the G peak position shift toward higher wavenumbers with temperature rise could be

seen from film 'α' to 'δ'. Again unlike the other films, for film 'δ' the *G* peak position remains invariant after 400℃ (similar to I_D/I_G changes in Figure 25(a)).

In view of these results it is plausible that during the annealing process first a clustering of the sp^2 bonded carbon atoms happens, without a change in relative sp^3 content of the films. The consequences of the sp^2 sites clustering is alteration in some physical properties, e.g. optical gap, electrical resistivity, and reduction in compressive stress [33, 34]. The I_D/I_G rise and the *G* line shift to higher wavenumbers with temperature evolution can be attributed to structural change of the films with conversion of a fraction of sp^3 bonds to sp^2 ; hence the films may be becoming graphitic clusters or layers [35]. Therefore, considering Figure 25(a) and (b), the limits of thermal stability of films 'α' – 'δ' can be assessed to be at temperatures below 400, 250, 200 and 200℃, respectively. The plateau stages seen for film 'δ' in Figure 25(a) and (b) at T≥400℃ may be attributed to the initiation of nano-crystalline graphite transformation to perfect graphite in which the decline in I_D/I_G ratio and shift of *G* peak to lower wavenumber is expected. The sharp reduction in hardness of film 'δ' at 350℃ can be correlated to this proposed transformation.

Comparison of the hardness reduction with temperature rise (Figure 23(b)) with the data in Figure 25(a) and (b), reveals that hardness reduction occurs even before the bulk structure of the films starts to chemically change. The clustering of sp^2 sites may happen before sp^3 to sp^2 transition where I_D/I_G starts to rise and the *G* peak begins to shift to higher wavenumbers. The sp^2 site clustering will result in reduction of compressive stress [34], which should be evident by *G* peak shift to lower wavenumbers [36]. However, except for the film 'β' and only when the temperature rises from RT to 100 ˚C, no shift of the *G* peak to lower wavenumbers could be seen from Figure 25(b).

The continuous hardness reduction with temperature rise seen in Figure 23(b), below the graphitization temperature of each film needs to be addressed as it may not be only due to stress reduction. The substrate material, Si (Single crystal), was also characterized using our coordinated mapping technique under different temperatures. The hardness and Young's modulus of Si against temperatures are presented in supporting information . The data shows that hardness of Si is not affected by temperature rise. Therefore, the hardness reduction for a-C films with temperature rise should be the dominant factor.

Another possibility is that the surface of the films is more temperature sensitive than the bulk. It should be noted that Raman is not a surface specific technique; whereas nanoindentation can be affected by changes that happen in surface layers. Therefore, using Raman spectroscopy, it is not possible to detect any changes that occur solely at the surface layers. Kelires [37] has studied the surface properties of ta-Cs by applying Monte Carlo simulations. His simulations showed that the sp^2 sites in the film are largely clustered. The atoms with sp^2 bonding have inhomogeneous distribution as a function of depth from the surface and the degree of clustering intensifies close surface region. It is expected to have a thin surface layer, roughly ~1.3 nm thick that displays stronger sp^2 characteristics compared to the bulk. This is because during deposition the outer atomic layer restructures as a graphite layer lying in the plane of the surface [37,38]. Keliries presumed that this sp^2-rich surface layer is intrinsic to the growth process due to deep subplantation. He also found that in the near-surface region, the defect formation energies are remarkably less than both diamond and graphite.

- <u>Topological studies</u>

If we propose that there is richer sp^2 content (high degree of clustering) near the surface region compared to the bulk during deposition for all a-C films rather than only for ta-C film, this hypothesis can be tested. Above a critical temperature depending to the sp^3 content of the bulk, the sp^3 to sp^2 conversion starts to happen. This conversion could be detected using Raman spectroscopy as Raman is bulk sensitive technique. However, the atoms near the surface with high degree of clustering may experience surface relaxation or oxidation with temperature rise, even before the graphitization happens in the bulk of the films. To investigate such a possibility, the changes in the surface roughness of the films during the temperature rise were measured and these are plotted in Figure 26. It is obvious that the surface roughness of films 'γ' and 'δ' dramatically increases with temperature rise from 350℃. While such a dramatic increase in surface roughness of film 'α' does not happen until the end of temperature-course.

The increase occurs for film 'β' upon a temperature rise from 400℃. The dramatic increase in surface roughness of film 'δ' happens right after a sharp decrease is seen in its hardness (Figure 23(b)) and Young's modulus (Figure 23(c)). For films 'β' and 'γ' it also happens after the slope of their curves of hardness and Young's modulus with T changes. The dramatic increase in surface roughness happens at temperatures higher than those for which Raman data shows the bulk chemical structure has started to change. The dramatic increase in surface roughness together with Raman spectra and hardness characterization indicate that the profound increase in surface roughness can be the result of structural changes in the bulk of these films. The inserted graph shows the changes in surface roughness of the films before the dramatic rise, in order to magnify the smaller changes in surface roughness that occur at T<350 for films 'β' – 'δ'. From the inserted graph, it can be seen that even the surface roughness of film 'α' gently increases with temperature rise from 350 to 400℃. The surface roughness of the films 'β' and 'γ' seems to start rising after 100℃, while for film 'δ' it starts to increase from RT. However,

these changes in surface roughness are small compared to the sharp increase which happens at T≥350℃. The rise in surface roughness of film 'β' – 'δ' at T<350℃ and for film 'α' at 350℃ may be the result of changes that happen in the surface and not in the bulk, considering that Raman spectra do not show structural changes in the bulk in this range. Our assumption is that the origin of changes in the surface is either surface relaxation in the top-most atomic layers or oxidization of the surface. In any case, the surface roughness change clearly shows that surface of the films endure some changes even before the chemical structure change in the bulk could be detected in their Raman spectra.

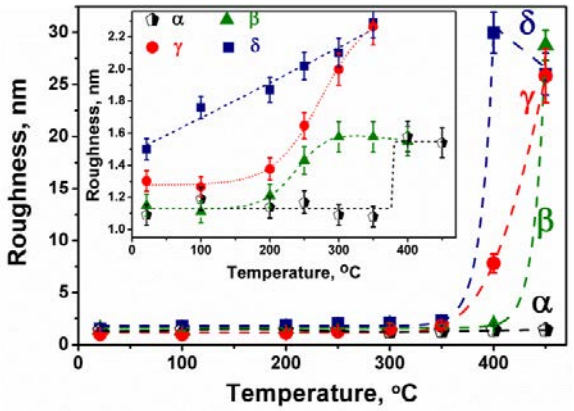

Figure 26. The changes in the surface roughness of films 'α' – 'δ' with temperature rise measured over a 25μm² square. The scanned areas were kept constant for each film until the end of the temperature-course. Each data is the average of tests on 2 samples. The inserted graph magnifies the small changes in surface roughness occurs at temperature below the temperature where dramatic rise is surface roughness of film 'β' – 'δ' happens.

To further investigate the possible surface changes with temperature rise, a nanoscratch test was carried out at different temperatures up 180℃ on film 'δ'. This film was selected for further analyses because it shows the most surface roughness change. A wide range of normal force (100 - 8000μN) was employed at each temperature to study the response of the film at different penetration depths. The friction coefficient and the normal displacement values derived from the nanoscratch test at different temperatures are shown in Figure 27(a) and (b), respectively. As expected, the normal displacement increases with increase in the applied normal force. From Figure 27(a), it is clear that friction coefficient for the scratches performed with very low normal force (100 μN), hence shallow scratch depths, strongly depends on the temperature, increasing dramatically with increasing temperature. This dependency gets weaker as we increase the normal force (the larger normal displacements). The friction coefficient remains almost constant with temperature rise when the scratch is performed using 5000 and 8000μN normal forces. Therefore, it can be concluded that the top surface layers are more sensitive to temperature compared to the bulk. The dramatic increase in friction coefficient for shallow scratches with temperature rise can be the consequence of the changes happening in surface layers. When the indentation tip moves at shallow depths (inside the top layers of the film) at elevated temperatures, the surface layers which have endured some changes, hence becoming softer, can gradually be accumulated in front of the moving tip. Therefore, higher lateral force will be needed to push the build-up material in front of the tip. When the indentation depth is increased, the softer part of the material on the surface is only a small portion of the material affected by scratch. Therefore, the build-up and increase of friction coefficient is not as significant as shallow scratch depths.

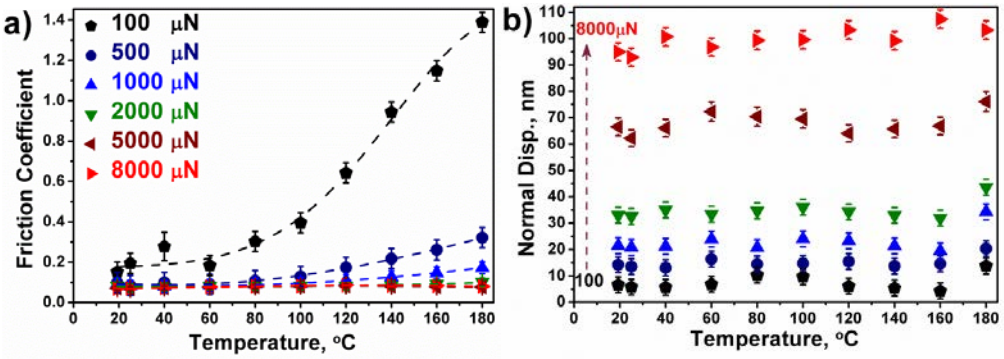

Figure 27 a) Friction coefficient against temperature of film 'δ' with different employed normal force (lines are guide for the eye) and b) Corresponding normal displacement to each employed normal force against temperature. The Data is the average of 4 tests for each point. (The gray arrow shows the increment in normal force).

To support our conclusions from the nanoscratch results, nanowear tests on film 'δ' at RT, 100 and 200℃ were performed with normal force of 780 μN. The dimension of the wear area was 2.5x2.5μm^2. The SPM images over 6x6μm^2 area and their corresponding cross section profiles are presented in Figure 28. From Figure 28, it can be seen that the wear depth increases from 3 to 5nm upon a temperature rise from RT to 100℃ showing that the surface layers become softer as the temperature rises. However, when the wear test is performed at 200℃, the surface topography changes dramatically due to the wear test and a build-up of material on one side (right hand in the image) of the worn area could be seen. Additionally the wear depth increased to 20nm. When the indentation tip moves from left to right, it sweeps the surface layers which have endured changes and have been softened. Therefore, this build-up of worn material is formed. Interestingly, the volume of these build-up increases in the direction of the wear scratch lines order (The tip scratches the film from left to right and then moves upward to do the next scratch) and the height of this build-up reaches up to 60 nm by the final wear scratch lines. This can indicate that the nature of the changes happening in the surface of the film is time dependent.

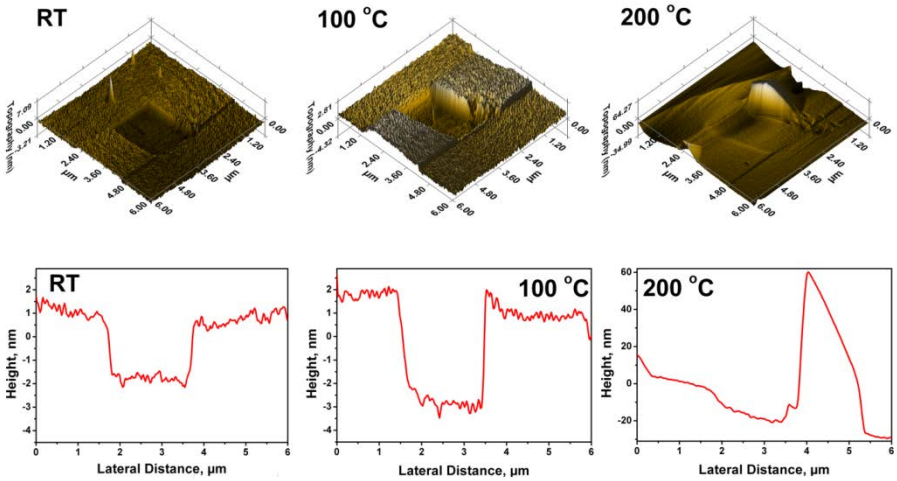

Figure 28 SPM images and cross section profiles for the wear test on sample 'δ' at RT, 100 and 200℃.

These observations all support the idea of the additional surface sensitivity to temperature rise, compared to the bulk and make it possible to explain the hardness reduction at temperatures below the critical temperature of onset of chemical structure evolution in the bulk. While the changes occurring in the surface can have significant impact on nanoindentation and surface roughness measurements, they cannot be detected by Raman spectroscopy as Raman is bulk sensitive technique. We could not definitively assign the origin of these changes at this stage, but we propose that it may be due to surface relaxation. To fully understand the mechanisms behind such surface sensitivity to temperature rise, more in-situ studies using surface sensitive techniques are needed.

3.6 Knowledge Transfer between the Collaborating Groups (Penn-CCU)

To strengthen collaboration between the two groups, since the last report, a graduate student from CCU, Yi Pan Lin, visited Prof. Carpick's lab and spent 2 weeks interacting with the postdoctoral researcher in Prof. Carpick's group, Dr. Rodrigo Bernal. This enabled the two groups to exchange information, methods, and knowledge, and to brainstorm on ideas. The student from CCU received extensive, hands-on training in the methods developed

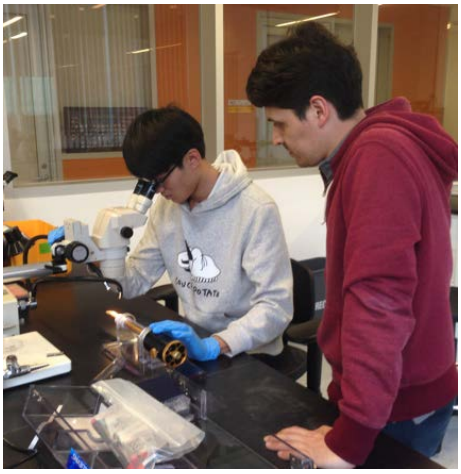

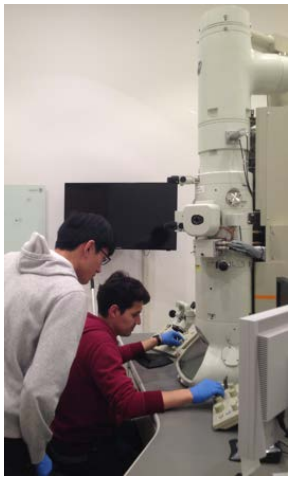

in Prof. Carpick's lab, and this enabled him to then to lead new experiments at CCU. Below are photographs from the visit.

4 List of Publications and Significant Collaborations that resulted from AOARD support

4.1 Papers Published in Peer-Reviewed Journals

1. Bernal, R.A., Chen, P., Schall, J.D., Harrison, J.A., Jeng, Y.-R. and Carpick, R.W. *Influence of Chemical Bonding on the Variability of Diamond-Like Carbon Nanoscale Adhesion*. **Carbon** 128, 267-276 (2018). http://dx.doi.org/https://doi.org/10.1016/j.carbon.2017.11.040

2. Shao, Y., Jacobs, T.D.B., Jiang, Y., Turner, K.T., Carpick, R.W. and Falk, M.L. *Multibond Model of Single-Asperity Tribochemical Wear at the Nanoscale*. **ACS Appl. Mat. Interf.** 9, 35333-35340 (2017). http://dx.doi.org/10.1021/acsami.7b08023

3. Liu, J., Jiang, Y., Grierson, D.S., Sridharan, K., Shao, Y., Jacobs, T.D.B., Falk, M.L., Carpick, R.W. and Turner, K.T. *Tribochemical Wear of Diamond-Like Carbon-Coated Atomic Force Microscope Tips*. **ACS Appl. Mat. Interf.** 9, 35341-35348 (2017). http://dx.doi.org/10.1021/acsami.7b08026

4. Mangolini, F., Krick, B.A., Jacobs, T.D.B., Khanal, S.R., Streller, F., McClimon, J.B., Hilbert, J., Prasad, S.V., Scharf, T.W., Ohlhausen, J.A., Lukes, J.R., Sawyer, W.G. and Carpick, R.W. *Effect of Silicon and Oxygen Dopants on the Stability of Hydrogenated Amorphous Carbon under Harsh Environmental Conditions*. **Carbon** 130, 127-136 (2018). http://dx.doi.org/https://doi.org/10.1016/j.carbon.2017.12.096

5. Rouhani, M., C.N., Hong, Jeng, Y.R. *In-situ thermal stability analysis of amorphous carbon films with different sp3 content*. **Carbon** 130, 401-409 (2018).
https://www.sciencedirect.com/science/article/pii/S0008622318300344

4.2 Papers published in peer-reviewed conference proceedings

N/A

4.3 Papers Published in Non-Peer-Reviewed Journals or in Conference Proceedings

N/A

4.4 Conference Presentations without Papers

Invited

- **Opening Session Keynote Talk:** *Academic-Industry Partnerships in Nanotechnology: Stories from the Trenches*, TechConnect World 2017 Innovation Conference, Washington, D.C., May 2017.

- **Keynote Speaker (*Yeau-Ren Jeng*):** *Nano-scale Mechanical Property Characterization: from a Tool of Mechanical Testing to Enabling Technology for Multidisciplinary Applications.* Nanobrücken 2018: A Nanomechanical Testing Conference, Germany, February 2018.

- *Influence of Chemical Bonding on the Variability of Diamond-Like Carbon Nanoscale Adhesion: An In-Situ TEM/Nanoindentation and Molecular Dynamics Study*. Symposium on *In situ* Methods for Probing Properties and Dynamics in Materials, Microscopy & Microanalysis Conference (M&M) Baltimore, MD, Aug. 2018.

- *Nanotribology: A Route to Global Energy Efficiency Invited Speaker*. National Academy of Engineering Annual Meeting, Section 10 (Mechanical Engineering), Washington, DC, Oct. 2017.

- *Emerging Trends in Nanotribology, and their Implications for Manufacturing*. Manufacturing Science and Engineering Conference (MSEC 2017), Los Angeles, CA, Jun. 2017

- *An Examination of DLC Adhesion and Wear using MD and in-situ Nanoindentation*. STLE Annual Meeting, Atlanta, GA, May 2017.

- *Nanoscale Studies of Mechanisms of Tribological Behavior*. DENSO, Kariya, Japan. Feb. 2017.

Contributed

- *An Examination of the Nature of Bonding during Indentation and Sliding using MD and in-situ Nanoindentation*. Gordon Research Conference on Tribology, Lewiston, ME, July 2018.

- *Nanoscale Adhesion of Sliding Silicon Contacts is Increased by Speed and Stress*. STLE Annual Meeting, Minneapolis, MN, May 2018.

4.5 Manuscripts Submitted but not yet Published

Milne, Z.B., Bernal, R.A. and Carpick, R.W. *Sliding History-Dependent Adhesion of Nanoscale Silicon Contacts Revealed by in Situ Transmission Electron Microscopy*. **Nature Materials**. Under review. (2018).

5 Interactions with industry or with Air Force Research Laboratory scientists or significant collaborations that resulted from this work.

- AFRL collaboration. Started with A. Voevodin (formerly at AFRL, now at U. North Texas) and C. Muratore, continuing with N. Glavin and C. Muratore – U. Dayton/AFRL
- Industrial collaborations with Advanced Diamond Technologies Inc. (Gurnee, IL, USA), and Adama Innovations LLC (Ireland), on the development of diamond nanostructures for AFM probes.
- Collaborating with Hysitron Inc. (Minneapolis, MN, USA) on developing *in situ* tools.

6 References

1. Starr, M.J. and Segalman, D.J. *An Empirical Relationship for Extrapolating Sparse Experimental Lap Joint Data*. **J. Appl. Mech.-T. ASME** 78 (2011). http://dx.doi.org/10.1115/1.4003769
2. Segalman, D.J. *Modelling Joint Friction in Structural Dynamics*. **Struct. Control Hlth.** 13, 430-453 (2006). http://dx.doi.org/Doi 10.1002/Stc.119
3. de Boer, M.P. and Mayer, T.M. *Tribology of MEMS*. **MRS Bulletin** 26, 302-304 (2001).
4. Becker, E.P. *Trends in Tribological Materials and Engine Technology*. **Trib. Int.** 37, 569-575 (2004).
5. Tung, S.C. and McMillan, M.L. *Automotive Tribology Overview of Current Advances and Challenges for the Future*. **Trib. Int.** 37, 517-536 (2004).
6. Doll, G.L. and Evans, R.D. *Solving Wind Turbine Tribological Issues with Materials Science*. **Materials Science and Technology Conference and Exhibition 2010, MS and T'10** 3, 2158-2169 (2010).
7. Kotzalas, M.N. and Doll, G.L. *Tribological Advancements for Reliable Wind Turbine Performance*. **Phil. Trans. A** 368, 4829-50 (2010). http://dx.doi.org/10.1098/rsta.2010.0194
8. Grillo, S.E. and Field, J.E. *The Friction of Natural and CVD Diamond*. **Wear** 254, 945-9 (2003).
9. Konicek, A.R., Grierson, D.S., Gilbert, P.U.P.A., Sawyer, W.G., Sumant, A.V. and Carpick, R.W. *Origin of Ultralow Friction and Wear in Ultrananocrystalline Diamond*. **Phys. Rev. Lett.** 100, 235502/1-4 (2008). http://dx.doi.org/10.1103/PhysRevLett.100.235502
10. Erdemir, A. and Donnet, C., *Tribology of Diamond, Diamond-Like Carbon, and Related Films*, in Modern Tribology Handbook, Vol. 2. (ed. B. Bhushan) 465-481 (CRC Press, Boca Raton, FL; 2001).
11. Chromik, R.R., Winfrey, A.L., Luning, J., Nemanich, R.J. and Wahl, K.J. *Run-in Behavior of Nanocrystalline Diamond Coatings Studied by in Situ Tribometry*. **Wear** 265, 477-89 (2008).
12. Hayward, I.P., Singer, I.L. and Seitzman, L.E. *Effect of Roughness on the Friction of Diamond on CVD Diamond Coatings*. **Wear** 157, 215-227 (1992).
13. Fontaine, J., Le Mogne, T., Loubet, J.L. and Belin, M. *Achieving Superlow Friction with Hydrogenated Amorphous Carbon: Some Key Requirements*. **Thin Solid Films** 482, 99-108 (2005). http://dx.doi.org/Doi 10.1016/J.Tsf.2004.11.126
14. Erdemir, A., Bindal, C., Fenske, G.R., Zuiker, C., Krauss, A.R. and Gruen, D.M. *Friction and Wear*

Properties of Smooth Diamond Films Grown in Fullerene + Argon Plasmas. **Diam. Relat. Mater.** 5, 923-931 (1996).

15. Jeng, Y.R. *Impact of Plateaued Surfaces on Tribological Performance*. **Trib. Trans.** 39, 354-361 (1996). http://dx.doi.org/Doi 10.1080/10402009608983538
16. Jeng, Y.R., Kao, W.C. and Tsai, P.C. *Investigation into the Mechanical Contact Behavior of Single Asperities Using Static Atomistic Simulations*. **Appl. Phys. Lett.** 91 (2007). http://dx.doi.org/10.1063/1.2776019
17. Jeng, Y.R., Lin, Z.W. and Shyu, S.H. *Changes of Surface Topography During Running-in Process*. **J. Tribology** 126, 620-625 (2004). http://dx.doi.org/10.1115/1.1759344
18. Jeng, Y.R. and Peng, S.R. *Elastic-Plastic Contact Behavior Considering Asperity Interactions for Surfaces with Various Height Distributions*. **J. Tribology** 128, 245-251 (2006). http://dx.doi.org/10.1115/1.2162557
19. Jeng, Y.R. and Peng, S.R. *Atomic Simulation of Contact Behavior During Sliding Inception of an Asperity*. **Wear** 276, 70-74 (2012). http://dx.doi.org/10.1016/j.wear.2011.12.002
20. Kunze, T., Posselt, M., Gemming, S., Seifert, G., Konicek, A.R., Carpick, R.W., Pastewka, L. and Moseler, M. *Wear, Plasticity, and Rehybridization in Tetrahedral Amorphous Carbon*. **Tribol Lett** 53, 119-126 (2014). http://dx.doi.org/10.1007/s11249-013-0250-7
21. Konicek, A.R., Grierson, D.S., Sumant, A.V., Friedmann, T.A., Sullivan, J.P., Gilbert, P., Sawyer, W.G. and Carpick, R.W. *Influence of Surface Passivation on the Friction and Wear Behavior of Ultrananocrystalline Diamond and Tetrahedral Amorphous Carbon Thin Films*. **Physical Review B** 85 (2012). http://dx.doi.org/10.1103/PhysRevB.85.155448
22. Kim, H.I., Lince, J.R., Eryilmaz, O.L. and Erdemir, A. *Environmental Effects on the Friction of Hydrogenated DLC Films*. **Tribol. Lett.** 21, 53-8 (2006).
23. Jacobs, T.D.B. and Carpick, R.W. *Nanoscale Wear as a Stress-Assisted Chemical Reaction*. **Nat Nanotechnol** 8, 108-112 (2013). http://dx.doi.org/Doi 10.1038/Nnano.2012.255
24. Jacobs, T.D., Wabiszewski, G.E., Goodman, A.J. and Carpick, R.W. *Characterizing Nanoscale Scanning Probes Using Electron Microscopy: A Novel Fixture and a Practical Guide*. **Rev. Sci. Instrum.** 87, 013703 (2016). http://dx.doi.org/10.1063/1.4937810
25. D. S. Grierson, A. V. Sumant, A. R. Konicek, T. A. Friedmann,J. P. Sullivan, R. W. Carpick, Thermal stability and rehybridization of carbon bonding in tetrahedral amorphous carbon, J. Appl. Phys. 107 (2010) 0335231-0335235.

26 A. C. Ferrari, J. Robertson, Interpretation of Raman spectra of disordered and amorphous carbon. Phys. Rev. B: Condens. Matter 61 (20) (2000) 14095-14106.

27 J. Robertson, Diamond-like amorphous carbon, Mater. Sci. Eng., R 37 (4) (2002) 129-281.

28 B. Druz, Y. Yevtukhov, I. Zaritskiy, Diamond-like carbon overcoat for TFMH using filtered cathodic arc system with Ar-assisted arc discharge, Diamond Relat. Mater. 14 (9) (2005) 1508 – 1516.

29 T.-Y. Kim, C. S. Lee, Y. J. Lee, K.-R. Lee, K.-H. Chae, K. H. Oh, Reduction of the residual compressive stress of tetrahedral amorphous carbon film by Ar background gas during the filtered vacuum arc process, J. Appl. Phys. 101 (2007) 023504.

30 M.K. Puchert, C.A. Davis, B.W. James, Gas plasma interactions in a filtered cathodic arc, J. Vac. Sci. Technol. A: Vac. Surf. Films 10 (1992) 3493-3498.

31 A. C. Ferrari, B. Kleinsorge, N. A. Morrison and A. Hart, Stress reduction and bond stability during thermal annealing of tetrahedral amorphous carbon, J. Appl. Phys. 85 (10) (1999) 7191.

32 N. Khamnualthong, K. Siangchaew, P. Limsuwan, Influence of thermal heating on diamond-like carbon film properties prepared by filtered cathodic arc, Thin Solid Films 544 (2013) 477–481.

33 J. Vetter, 60 years of DLC coatings: Historical highlights and technical review of cathodic arc processes to synthesize various DLC types, and their evolution for industrial applications, Surf. Coat. Technol. 257 (2014) 213–240.

34 A.C. Ferrari, S. E. Rodil, J. Robertson, W. I. Milne, Is stress necessary to stabilise sp^3 bonding in diamond-like carbon?, Diamond Relat. Mater. 11 (2002) 994.

35 R. Hatada, S. Flege, K. Baba, W. Ensinger, H.-J. Kleebe, I. Sethmann, et al. Temperature dependent properties of silicon containing diamondlike carbon films prepared by plasma source ion implantation. J. Appl. Phys. 107 (2010) 0833071-0833076.

36 Y. Miki, A. Nishimoto, T. Sone, Y. Araki, Residual stress measurement in DLC films deposited by PBIID method using Raman microprobe spectroscopy, Surf. Coat. Technol. 283 (2015) 274–280

37 P. C. Kelires, Surface properties of diamond-like amorphous carbon. J. Non-Cryst. Solids 227–230 (1998) 597–601.

38 C. Casiraghi, A. C. Ferrari, R. Ohr, A. J. Flewitt, D. P. Chu, J. Robertson, Dynamic Roughening of Tetrahedral Amorphous Carbon. Phys. Rev. Lett. 91 (22) (2003) 2261041-4.

DISTRIBUTION A: Approved for public release; distribution unlimited